SPECTROSCOPIC STUDY
OF
TRANSITION METAL COMPOUNDS

A Thesis Submitted to the
College of Graduate Studies and Research
in Partial Fulfillment of the Requirements
for the Degree of Master of Science in the
Department of Physics and Engineering Physics
University of Saskatchewan
Saskatoon

by

Sanjukta Choudhury

PERMISSION TO USE

In presenting this thesis in partial fulfillment of the requirements for a Postgraduate degree from the University of Saskatchewan, I agree that the Libraries of this University may make it freely available for inspection. I further agree that permission for copying of this thesis in any manner, in whole or in part, for scholarly purposes may be granted by my supervisor Dr. Alexander Moewes or, in his absence, by the Head of the Department or the Dean of the College in which my thesis work was done. It is understood that any copying or publication or use of this thesis or parts thereof for financial gain shall not be allowed without my written permission. It is also understood that due recognition shall be given to me and to the University of Saskatchewan in any scholarly use which may be made of any material in my thesis.

Requests for permission to copy or to make other use of material in this thesis in whole or part should be addressed to:

Head of the Department of Physics and Engineering Physics

University of Saskatchewan

Saskatoon S7N 5E2

Saskatchewan

Canada

ABSTRACT

The electronic structure of some transition metal compounds, specifically, Ca-doped $LaMnO_3$, fundamental Mn oxides (MnO, Mn_2O_3, Mn_3O_4, and MnO_2), and Fe-doped ZnO is studied using a combination of soft X-ray spectroscopy and atomic multiplet calculations. X-ray absorption spectroscopy (XAS) and X-ray emission spectroscopy (XES) are used as experimental tools to probe the unoccupied and occupied partial density of electronic states, respectively.

Ca-doped $LaMnO_3$ perovskites have attracted great attention due to their colossal magnetoresistance and a wide range of magnetic and structural transitions. The magnetic and charge transport properties of these perovskites are directly related with Mn 3*d*-occupancy or Mn-valency and therefore, an investigation of the Mn-valence at Ca-doped $LaMnO_3$ system is important. In this system, the Mn-valency is generally considered as a mixture of Mn^{3+} and Mn^{4+}. But my research suggests the presence of Mn^{2+} at the surface of Ca-doped $LaMnO_3$ samples. It is observed that increasing Ca-doping decreases Mn^{2+} concentration, and conversely, increases Mn^{3+} concentration. High temperature annealing at 1000 °C in air leads to the full reduction of surface Mn^{2+}. Mechanisms for these observations are proposed in this study.

Mn oxides (MnO, Mn_2O_3, Mn_3O_4, and MnO_2) are often used as reference standards for determining the Mn-valency in Mn-related complex systems and therefore a detailed understanding of their electronic structure is necessary. The Mn $L_{2,3}$ XAS and O *K* XAS are measured for the four Mn oxides consisting of three common Mn oxidation states (Mn^{2+} in

MnO, Mn^{3+} in Mn_2O_3, mixture of Mn^{2+} and Mn^{3+} in Mn_3O_4, and Mn^{4+} in MnO_2). A significant energy shift with a systematic trend is observed in measured Mn $L_{2,3}$ and O K absorption edges. These energy shifts are identified as a characteristic shift for different Mn oxidation states. Mn $L_{\alpha,\beta}$ Resonant Inelastic X-ray Scattering (RIXS) spectroscopy is demonstrated as a powerful tool in describing low energy excitations, e.g. *d-d* excitations and charge-transfer excited states in Mn oxides. For the first time, a RIXS study of Mn_2O_3, Mn_3O_4, and MnO_2 is accomplished. Atomic multiplet calculations are used to successfully reproduce the energy positions and intensity variations of *d-d* excitation peaks observed in the experiment, and thus to describe the experimental RIXS spectra.

Finally, the local electronic structure of Fe implanted ZnO samples, a useful diluted magnetic semiconductor for spintronics, is investigated to shed light on the existing debate about the origin of ferromagnetism in these materials. Fe $L_{2,3}$ XAS reveals that doped Fe ions are present in both Fe^{2+} and Fe^{3+} valence states. A combined theoretical and experimental study shows that doped ions are incorporated into Zn-sites of ZnO in tetrahedral symmetry. Fe L_3-RIXS measurements demonstrate that a high Fe-ion dose of 8×10^7 cm^{-2} causes formation of FeO clusters, while low dose samples exhibit more free carriers.

ACKNOWLEDGEMENTS

I am grateful to my supervisors Prof. Alexander Moewes and Dr. Gap Soo Chang for their constant encouragement and invaluable guidance to make my dream a reality. Directions and contributions from my advisory committee members are also gratefully acknowledged. My sincere thanks to Tom Regier, beamline scientist of the SGM beamline at CLS, as well as Wanli Yang and Jonathan Denlinger, beamline scientists of the beamline 8.0.1 at ALS for their helpful support during measurements. Help and support from all of the Beamteam members is greatly valued and appreciated. I would like to express gratitude and thanks to my family for their encouragement and support, without their directions and guidance I would not be the person I am today. Financial support from the Natural Sciences and Engineering Research Council of Canada (NSERC) and the Canada Research Chair program is gratefully acknowledged. Work at the Advanced Light Source at Lawrence Berkeley National Laboratory is supported by the US Department of Energy (Contract DE-AC03-76SF00098).

TABLE OF CONTENTS

LIST OF TABLES

Table Page

LIST OF FIGURES

Figure Page

Figure Page

LIST OF ABBREVIATIONS

ALS	Advanced Light Source
BL 8.0.1	Beamline 8.0.1
BSE	Basis State Edition
CB	Conduction Band
CLS	Canadian Light Source
CMR	Colossal Magnetoresistance
DE	Double Exchange
DMS	Dilute Magnetic Semiconductor
EELS	Electron Energy Loss Spectroscopy
HEG	High Energy Grating
HF	Hartree-Fock
LEG	Low Energy Grating
LINAC	Linear Accelerator
MCP	Multiple Channel Plate
MEG	Medium Energy Grating
NEXAFS	Near Edge X-ray Absorption Fine Structure
NXES	Non-resonant X-ray Emission Spectroscopy
PCA	Principal Component Analysis
RF	Radio Frequency
RIXS	Resonant Inelastic X-ray Scattering
RKKY	Ruderman, Kittel, Kasuya and Yoshida
SCF	Self Consistent Field

SGM	Spherical Grating Monochromator
SXF	Soft X-ray Fluorescence
TEP	Thermo Electric Power
TEY	Total Electron Yield
TFY	Total Fluorescence Yield
TM	Transition Metal
UHV	Ultra High Vacuum
VB	Valence Band
XAS	X-ray Absorption Spectroscopy
XANES	X-ray Absorption Near Edge Structure
XES	X-ray Emission Spectroscopy

CHAPTER 1
INTRODUCTION

Soft X-ray spectroscopy using synchrotron radiation is employed in this study to determine the electronic structure of three transition metal compounds. Soft X-ray absorption spectroscopy (XAS) and emission spectroscopy (XES) probe the partial density of unoccupied and occupied states, respectively. Atomic multiplet calculations are used to theoretically calculate the experimental spectra, and thus to facilitate the analysis of the experimental data. A combined analysis of experimental and theoretical data often provides valuable information that is not attainable solely by the experiment.

A study of the electronic structure of Ca-doped $LaMnO_3$ to investigate the Mn-valency is one of the reported studies in this thesis. Extensive research interest on perovskite manganites has been triggered by their distinctive magnetic, transport, and magnetoresistive properties, for instance, magnetic phase transitions, metal-insulator transitions, and colossal magnetoresistance (CMR) [1]. Perovskite manganites are usually characterized by the general formula $(A^{3+})_{1-x}(B^{2+})_xMn(O^{2-})_3$, where '*A*' represents a rare-earth ion (i.e., La, Nd, Pr etc.) and '*B*' stands for an alkaline earth cation (i.e., Ba, Ca, Sr etc.). Oxygen is strongly electronegative and therefore replacing trivalent '*A*'-sites with the corresponding amount of divalent '*B*'- sites leads to a change in Mn 3*d*-occupancy. For the pure $LaMnO_3$ compound, the ionic composition is $La^{3+}Mn^{3+}O_3^{-6}$. Replacement of some trivalent La by divalent Ca, Sr, or Ba causes the corresponding amount of Mn^{3+} to become Mn^{4+}. Thus these materials exhibit doping-dependent Mn valency and consequently, the novel properties of these manganites are also a function of the dopant concentration *x*. Ca-doped $LaMnO_3$ is one of the typical manganite perovskite systems, where substitution of divalent Ca^{2+} in the trivalent La^{3+} site leads to a mixed Mn^{3+}/Mn^{4+} valence state [2]. Double exchange (DE) theory [2] was proposed to qualitatively explain the close interplay between magnetic order and concomitant metal-insulator transition in these compounds. There are a number of previous studies, which express concerns about the surface electronic structure of $La_{1-x}Ca_xMnO_3$ materials. It has been reported that the surface chemical composition of these materials is different with respect to the bulk due to segregation effects [3]. A substantially different temperature dependence of

the surface boundary magnetization [4] and insulating character at the surface boundary [5, 6] compared to the bulk is reported. Magneto-optical measurements show the presence of surface layers 5 to 20 Å with suppressed magnetic properties in $La_{2/3}Ca_{1/3}MnO_3$ thin films [7]. According to theoretical predictions, the DE-interaction is weaker at the surface of manganites due to the reduced crystal symmetry [8]. Sometimes surface modifications have been attributed to the defects or stoichiometry at the surface boundaries [9]. The observed modification of the surface magnetic properties with respect to the bulk has to be taken into account for applications such as magnetoelectronic devices, e.g. magnetic tunneling junctions [10]. There are also much conflicting data regarding the Mn-valence in manganese perovskites. X-ray absorption spectroscopy and resonant photoemission study on $La_{0.7}Sr_{0.3}MnO_3$ and $La_{2/3}Ca_{1/3}MnO_3$ thin films [11-13] recently reported the presence of Mn^{2+} at the sample surface but in ref. 13 it is described that the presence of Mn^{2+} is not restricted only to the surface of $La_{2/3}Ca_{1/3}MnO_3$ thin films but extended throughout the volume of the sample. Thermoelectric power (TEP) study of $La_{1-x}Ca_xMnO_{3+\delta}$ [14] suggests a charge disproportionation model "$2\ Mn^{3+} \rightarrow Mn^{2+} + Mn^{4+}$" to explain the experimental observation. This set of conflicting data as well as general interest regarding the change of surface electronic structure as a function of doping concentration demand further investigation of the Mn-valence state in $La_{1-x}Ca_xMnO_3$ perovskites. In the present study, Mn 2*p* and O 1*s* XAS measurements of $La_{1-x}Ca_xMnO_3$ (x = 0.20, 0.21, 0.23, and 0.25) single crystals are performed, which probe the unoccupied partial density of Mn 3*d* and O 2*p* states, respectively. Surface sensitive and bulk sensitive XAS measurements are compared to show that the surface electronic structure of $La_{1-x}Ca_xMnO_3$ is different with respect to the bulk. Details of this study are reported in section 5.1 of this document.

An electronic structure study of four fundamental Mn oxides (MnO, Mn_2O_3, Mn_3O_4, and MnO_2) using soft X-ray spectroscopy is reported in this thesis. Mn oxides are widely used as reference materials in various studies of Mn-related strongly correlated systems. Hence, it is important to obtain a good understanding of their electronic structure. Also, Mn oxides are very common in nature and they exist in various forms of Mn-valency. It is required to identify them in terms of their Mn-valence states as different *d*-occupancy contributes significantly to the variation in their physical properties, for instance, magnetic, electronic,

and charge transport etc. In spite of their obvious importance in physical and environmental sciences, very little electronic structure study has been reported on these oxides. Though a number of studies are found on MnO [15 - 17], no attempts have been made to report XES of the other three oxides. In this thesis, XAS and XES study of all four oxides are reported with the atomic multiplet calculations of all experimental spectra. Mn 2*p* and O 1*s* XAS are sensitive to Mn-valency [18 - 21] and therefore are used to distinguish different Mn-valence states such as Mn^{2+}, Mn^{3+}, and Mn^{4+}. High quality spectra with their interpretation using atomic multiplet calculation are reported to establish Mn oxides as standard reference materials. Mn $L_{\alpha,\beta}$ Resonant Inelastic X-ray Scattering (RIXS) are measured by selecting photon energies near the Mn $L_{2,3}$ absorption edges for these four oxides to probe low-lying electronic excited states such as, intra-atomic *d-d* excitations and interatomic charge transfer excitations. Atomic multiplet calculations are used to theoretically calculate the experimental *dd*-peaks. Both energy positions of the *dd*-peaks and intensity variations are reproduced well in the calculation. Details of this study are found in the section 5.2 of this thesis.

Finally, a soft X-ray study of Fe-doped ZnO, which is known as a potential transition metal compound for spintronics, is also part of this thesis. Semiconductor technology uses the charge of an electron as a foundation of information processing, and physics of magnetism uses the spin of an electron for information storage and retrieval. Efforts to combine both semiconductivity and magnetism in a single material, give rise to a new group of material called dilute magnetic semiconductors (DMSs), which are the building block of modern spintronics. In DMSs, both charge and spin of an electron are exploited and thus they yield interesting multiple device applications, for instance, spin-transistors, spin-valves, magnetic random-access-memory, spin-polarized light emitting diodes, and chips that integrate memory and microprocessor functions. The design of DMSs involve different semiconductor hosts, which generally can be divided into two groups; oxide-based DMSs, e.g. ZnO, TiO_2, SnO_2 doped with transition metals (TMs) and non-oxide based DMSs like DMS based on III-V semiconductors such as GaAs, InAs etc. Oxide-based DMSs are more advantageous than their counterpart because they exhibit optical transparency, wider band gap, and high n-type carrier concentration. Among other semiconducting oxides, ZnO is very promising because it has the potential of multifunctionality such as optical, semiconducting, magnetic, and

electromechanical properties. Also, ZnO is piezoelectric [22] with the wide band gap of ~3.4 eV, which is tunable over a large energy range by exploiting appropriate doping [22]. In the area of spintronics, ZnO doped with TMs (Mn, Fe, Co, Ni) are of great interest because they are reported to exhibit ferromagnetism at room temperature, which is a key requirement for realizing spintronic devices. Room temperature ferromagnetism has been reported in Mn-doped ZnO [23], Fe-doped ZnO [24], Co-doped ZnO [25], Ni-doped ZnO [26] and others. However, the origin of ferromagnetism in TM-doped ZnO is still under debate. To explain the observed room temperature ferromagnetism in TM-doped ZnO, several theoretical descriptions e.g. RKKY-Zener interaction [27, 28], double exchange-Zener interaction [29], theory based on interaction between bound magnetic polarons [30], and disorder defects [31-33] have been taken into account but none of those successfully resolved the issue. The controversy exists about the issue whether ferromagnetism in the ZnO-based DMS is carrier-induced (intrinsic) or due to the formation of TM-related secondary phases (extrinsic). As the atomic size of Fe^{2+}/Fe^{3+} is similar to that of Zn^{2+}, we can simply expect that the Zn site in traditional zinc blende or wurtzite structure of ZnO is substituted by the Fe dopant. In the present work, XAS and XES are used to study the local electronic structure of Fe ions in Fe-implanted ZnO samples prepared by Fe ion implantation. Theoretical calculations of Fe 2*p* XAS spectra using the atomic multiplet code are used to determine the coordination environment of doped Fe-ions in the ZnO matrix. Details of this study are reported in section 5.3 of this thesis.

Regarding the structure and contents of this thesis, there are six chapters in total. Chapter 1 gives background and motivation of the research. In Chapter 2, a short description of the synchrotron sources is presented with an emphasis on the spherical Grating Monochromator (SGM) beamline at the Canadian Light Source (CLS) and beamline 8.0.1 at the Advanced Light Source (ALS) as these are used in this research. Chapter 3 describes the experimental techniques used in this study with their advantages and shortcomings. In Chapter 4, a description of the theories used in calculations is provided with limited mathematical derivations. Chapter 5 gives details of the measurements, analysis, results, and discussions to report the study of three transition metal compounds. Finally, Chapter 6 summarizes the study.

CHAPTER 2
SYNCHROTRON SOURCES

A synchrotron is a modern experimental research facility that provides bright, inherently polarized, highly focused, and tunable electromagnetic radiation over a large continuous electromagnetic spectrum to study the structure and dynamics of a wide variety of materials. The first observation of synchrotron radiation was made in 1947, at the General Electric Research Laboratory in Schenectady, NY. The story of the advent of synchrotron radiation is described in the publication of H. C. Pollock, titled '*Discovery of synchrotron radiation*' [34]. Since this discovery, synchrotron sources have gone through tremendous modifications in order to achieve optimized radiation quality and usage. In the synchrotron light sources, a magnetic field forces electron with relativistic speed to confine in an approximately circular orbit with acceleration directed towards the center of the orbit. The magnetic field does not change the magnitude of the velocity of electrons but changes their direction, which results in emission of electromagnetic radiation. The wavelength of the emitted radiation is a function of the energy of electrons and the strength of magnetic field. Relativistic speed of the electron is important because a non-relativistic ($v/c << 1$) electron emits less bright radiation in a non-directional manner while for relativistic electrons the emission pattern forms a tangentially outward narrow cone of radiation with dramatic increase of radiation power [35]. The produced radiation is highly collimated and the angular distribution of the emitted radiation is typically expressed by $1/\gamma$, where γ represents the Lorentz contraction factor, which is defined in terms of the velocity (v) and the speed of light as follows [35].

$$\gamma = \frac{1}{\sqrt{1-\frac{v^2}{c^2}}} \tag{2.1}$$

The power of the emitted synchrotron radiation is determined by the characteristics of the storage ring. It is estimated by the following expression 2.2 [35].

$$P[kW] = 8.86 \times 10^{-2} \frac{E^4[GeV] I[mA]}{\rho[m]} \tag{2.2}$$

Where P is the emitted power, E is the electron energy, I stands for the storage ring current, and ρ represents the radius of curvature of the storage ring. Synchrotron radiation travels tangentially away from the storage ring to the different experimental endstations. Each experimental station is designed and equipped for specific experimentation techniques, where the users can control the wavelength of the radiation as required by their experiment.

Components of a synchrotron source typically include an electron gun, a linear accelerator, a booster ring, a storage ring, beamlines, and experimental endstations. Figure 2.1 obtained from the CLS website [36] shows a schematic diagram of the synchrotron components.

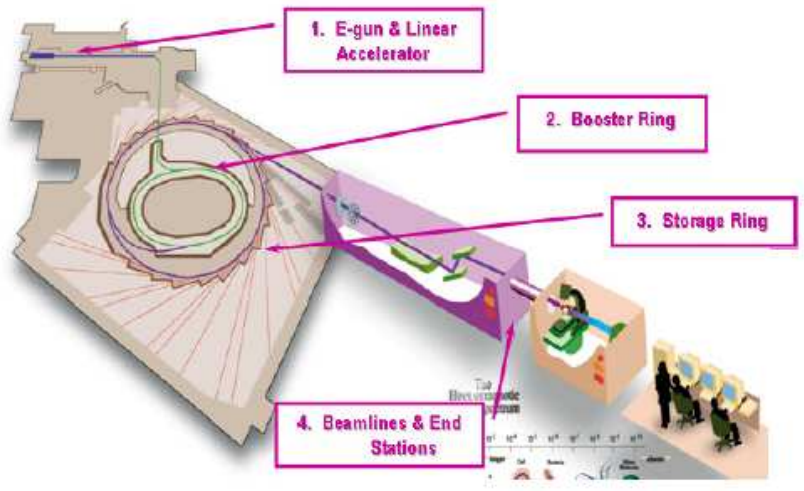

Figure 2.1 A schematic diagram of the components of synchrotron at CLS. (Figure from ref. 36).

2.1 Electron Gun

An electron gun at the CLS is a tungsten-oxide disk cathode. A high voltage (approximately 200,000 volts) of electricity passes through it until electrons are emitted [36]. A positively charged screen placed in front of the cathode attracts the emitted electrons and thus generates

an intense beam of high energy electrons. These electrons are then accelerated toward the linear accelerator (LINAC) by an extremely high potential.

2.2 Linear Accelerator (LINAC)

In the LINAC, electrons are bombarded by the radio frequency (RF) radiation causing them to gain energy and to bunch together. At the CLS, a 2856 MHz microwave radio frequency field causes electrons to gain approximately 250 MeV of energy with which they travel at 99.9998% of the speed of light [36]. These electron bunches are the final output of the LINAC, and subsequently injected into the booster ring.

2.3 Booster Ring

The function of a booster ring is to further energize the electrons and they travel in a circular trajectory. The circular structure of the booster ring causes electrons to pass through the RF cavity in each cycle and tuned microwave radiation is used to continue ramping up the energy of the electron bunches. At the CLS, due to the 2856 MHz microwave field in the RF cavity, the circulating electron receives a boost in energy from 250 MeV to 2900 MeV [36]. Subsequently, when the target energy is achieved (approximately 1.9 GeV at the ALS and 2.9 GeV at the CLS), electron bunches are ejected into the storage ring, where they circulate for many hours generating synchrotron radiation at every turn.

2.4 Storage Ring and Insertion Devices

At the CLS, the booster ring supplies 2.9 GeV electrons into the 171 m (circumference) storage ring through an injection system [36]. Modern storage rings contain many straight sections for insertion devices though early storage rings were basically circular. The CLS storage ring consists of a series of 12 straight sections each with two dipole magnets and also a series of 6 quadrupole and 3 sextupole magnets in order to narrow the electron beam [36]. Some straight sections of the storage ring are designed to assemble special magnetic structures known as insertion devices. These magnetic structures include bending magnets, undulators, and wigglers, which are described in the section below. At each turn of the storage ring, there is a port for produced photons to travel to the experimental station. The electrons

eventually lose energy and an additional RF system is installed inside the storage ring, which maintains the energy level of the circulating beam.

2.5 Insertion Devices (Bending Magnets, Undulators, and Wigglers)

A bending magnet causes electron beam to deflect from their straight path and thus to follow a desired trajectory to travel through the storage ring. The deflection due to the magnetic field of the bending magnet results in a tangential emission of synchrotron radiation. The emitted radiation consists of a broad spectrum with a typical angular distribution of $1/\gamma$. Bending magnets are characterized by a quantity known as their critical photon energy (E_c). E_c of a bending magnet radiation is defined as the energy that divides the bending magnet radiation spectrum into two halves of equal radiated power. The spectral intensity decreases rapidly for photon energies above the value of E_c. In practical units, the critical photon energy is given by the expression 2.3 [35].

$$E_c(keV) = 0.6650 B_0(T) E_e^{\,2}(GeV) \tag{2.3}$$

Where E_c is the critical photon energy, B_0 is the magnetic field of the bending magnet, and E_e stands for the electron beam energy.

An undulator consists of a complex periodic array of small magnets and is positioned in the straight sections of the storage ring. The electron beam passing through this magnetic structure undergoes periodic deflections transversely to the direction of their forward motion. This acceleration of the electron beam causes synchrotron radiation to be emitted. An undulator is designed for the coherent interference to occur. The emitted radiation from the consecutive periods constructively interferes to produce a very intense quasi-monochromatic beam of radiation. Undulators are usually used in a soft X-ray beamline that require a relatively small energy range of radiation and higher flux.

Wigglers are similar to undulators but consist of fewer magnetic poles. The magnetic field of a wiggler is stronger in comparison to an undulator, resulting in a relativistic transverse motion of an electron beam. Wigglers are not designed for coherent interference among the

radiation from each set of magnetic poles but these are designed to increase the intensity of the high energy part of the synchrotron radiation. An undulator produces a narrower range of energies with higher intensities while a wiggler gives a wide range of high energy radiation and is usually used for hard X-ray beamlines that require a broad range of X-rays.

Figure 2.2 shows a comparison among the outputs of the three insertion devices. Undulators and wigglers are often described by the *K*-parameter, which is given by the following expression [35].

$$K = \frac{e}{2\pi m_e c}\lambda_u B \tag{2.4}$$

Where m_e is the rest mass of electron, c is the speed of light, λ_u is the periodic length of insertion device, and B is the magnetic field inside the insertion device. For a wiggler, K is much greater than 1, whereas for undulators K is approximately equal to 1.

Tunability of synchrotron radiation is achieved by changing the gap between magnets, which changes the magnetic field of the insertion device. Decreasing the gap will increase the magnetic field of the device and increasing the gap will decrease the magnetic field. This changes in the magnetic field causes the parameter K (equation 2.4) to change, which finally causes the energy of the produced synchrotron radiation to change. In practical units the energy of the n^{th} harmonic of the synchrotron radiation produced from an insertion device is given by the following expression (2.5) [35].

$$E_n = 0.950\frac{nE^2[GeV]}{\lambda_p[cm]\left(1+\frac{K^2}{2}\right)}; \qquad n = 1, 2, 3\ldots \tag{2.5}$$

Where E is the ring energy, λ_p is the characteristic period length for the insertion device, and K is the parameter defined in the expression 2.4. Higher harmonics are used to extend the useful energy range of the device, because, practically there are some limitations to the

possible variations of the magnetic field of the insertion devices. Only the odd numbered harmonics are used in the experiment, as the even numbered harmonics have a node along the axis of the undulator and therefore radiation will be off-axis [35].

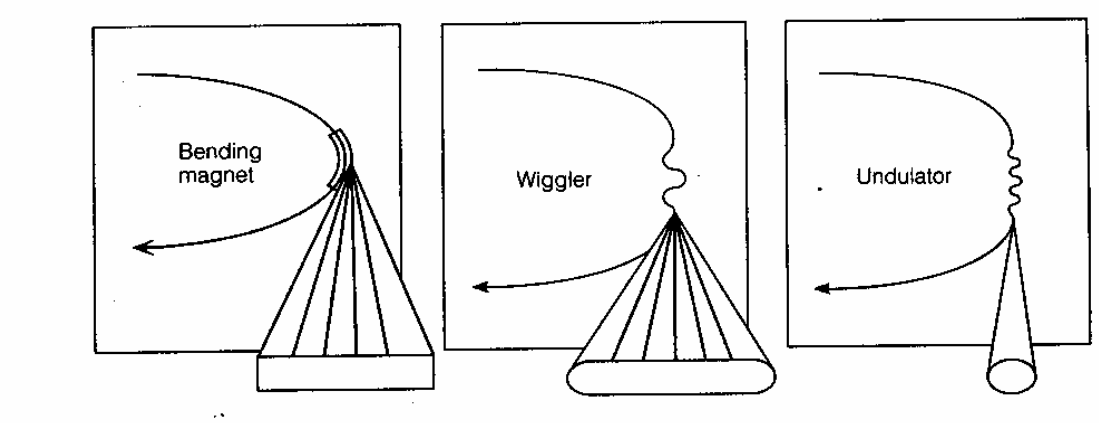

Figure 2.2 Comparison of the outputs of Insertion devices (Figure from ref. 36).

2.6 Beamline Description

Spectroscopic measurements reported in this thesis are performed at the Spherical Grating Monochromator (SGM) beamline of the Canadian Light Source (CLS), University of Saskatchewan and at the beamline 8.0.1 of the Advanced Light Source (ALS), Lawrence Berkeley National Laboratory, USA. Brief descriptions of the beamlines are given in the following sections.

2.6.1 SGM Beamline at the Canadian Light Source (CLS)

The Canadian Light Source (CLS) is the smallest of the newer synchrotron sources, which is operating at 2.9 GeV. It consists of a 250 MeV LINAC, a 2.9 GeV booster ring, and a compact, double-bend lattice storage ring with a superconducting RF cavity. Details of the synchrotron design and operation can be found in refs. 37 and 38.

The Spherical Grating Monochromator (SGM) beamline at the CLS is an undulator based beamline operating over the soft X-ray energy range of 250 eV to 2000 eV with a resolving power greater than 10^4 for the energies below 800 eV [39]. Figure 2.3 shows a schematic

layout of this beamline, which is drawn according to the one found in the CLS activity report, 2007 [40]. The SGM beamline employs two horizontal deflecting mirrors and one vertical focusing mirror to direct the radiation from the undulator through the entrance slit and then onto the interchangeable gratings of the monochromator. The SGM monochromator is comprised of three diffraction gratings and experimenters are allowed to choose one depending on their desired energy range. The line density of the three gratings is 600, 1100, and 1700 lines/mm for LEG, MEG, and HEG, respectively. Monochromatized radiation then passes through an exit slit of variable width. The slits and gratings are arranged in a way that they obey Rowland circle condition; i.e., the two slits and one of the three interchangeable gratings are located along a circle of radius R/2, where R is the radius of curvature of the spherical grating. A pair of toroidal refocusing mirrors is used to focus the beam onto the sample to be studied. Details of the beamline can be found in ref. 39.

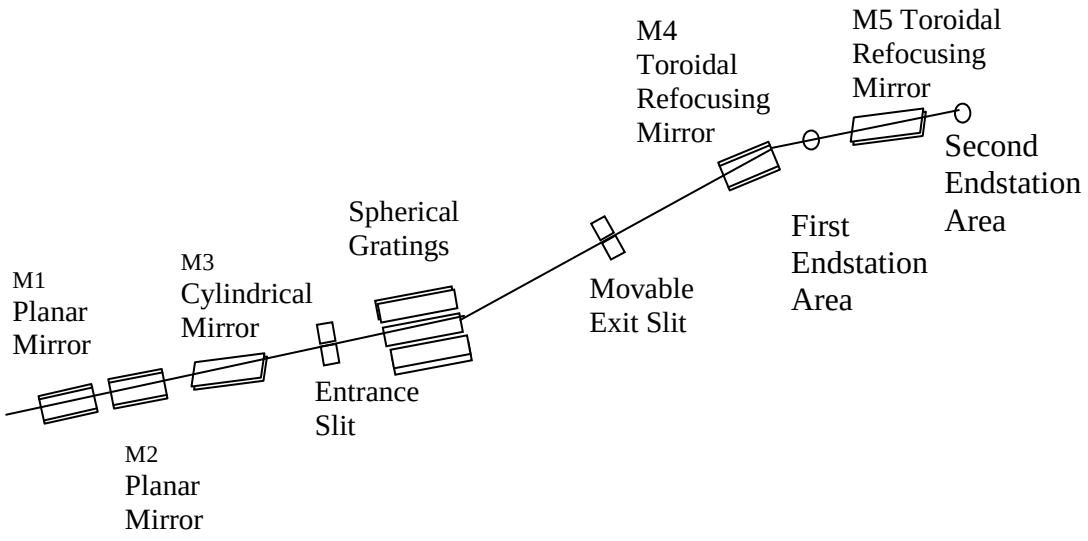

Figure 2.3 Schematic layout of the SGM beamline at the Canadian Light Source (CLS) [40].

2.6.2 Beamline 8.0.1 at the Advanced Light Source (ALS)

Beamline 8.0.1 at the ALS is a U5.0 undulator based beamline operating over the spectral range of 70 - 1200 eV. Undulator consists of 89 poles with a period of 5.0 cm allowing

variable 1st, 3rd, and 5th harmonics [41]. High resolution spherical grating monochromator operates in a resolving power of 2000 with three interchangeable gratings [41]. Desired resolution of the monochromator can be selected by choosing the width of the entrance slit and the exit slit. A soft X-ray fluorescence (SXF) detector is mounted on a movable platform that slides on air bearings. The resolving power of the spectrometer for fluorescence measurements is 400 [41]. Figure 2.4 shows a schematic layout of the beamline 8.0.1 at ALS obtained from the ALS website [42]. A brief description of the beamline monochromator of the beamline 8.0.1 and the SXF spectrometer at the endstation is provided in the following sections.

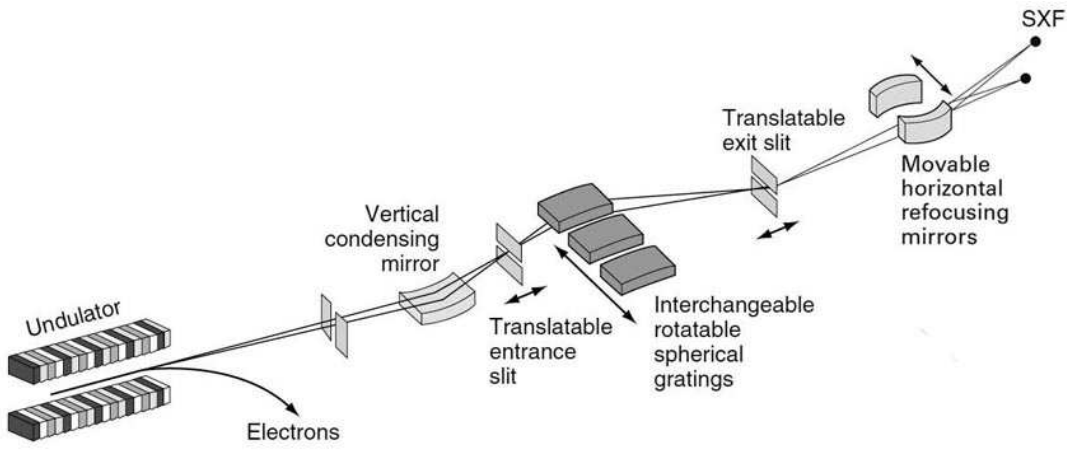

Figure 2.4 Schematic layout of the beamline 8.0.1 at the ALS (Figure from ref. 42).

2.6.2.1 The Monochromator

The monochromator at beamline 8.0.1 uses spherical gratings in grazing incidence geometry. Figure 2.5, obtained from the beamline technical data sheet [42], displays the BL 8.0.1 monochromator characteristics for the experimenters. The major components of the BL 8.0.1 monochromator are three interchangeable gratings, a water cooled movable entrance slit, an uncooled movable exit slit, and a horizontal refocusing mirror [41]. Using the water-cooled SiC vertical condensing mirror, undulator radiation is focused onto the water-cooled movable entrance slit. Then the radiation goes into the grating tank containing three water-cooled

holographically ruled laminar diffraction gratings of line spacing 150 (LEG), 380 (MEG), and 925 (HEG) lines/mm, which allow energies from 80 eV to 1400 eV to be selected [41]. The optimized focusing can be achieved by changing the width of the entrance and the exit slit to satisfy the Rowland geometry. This geometry requires that these three components are on a circle with a radius equal to one-half of the radius of curvature of the spherical diffraction grating. A horizontal refocusing mirror is installed to narrow down the spot size toward the SXF endstation.

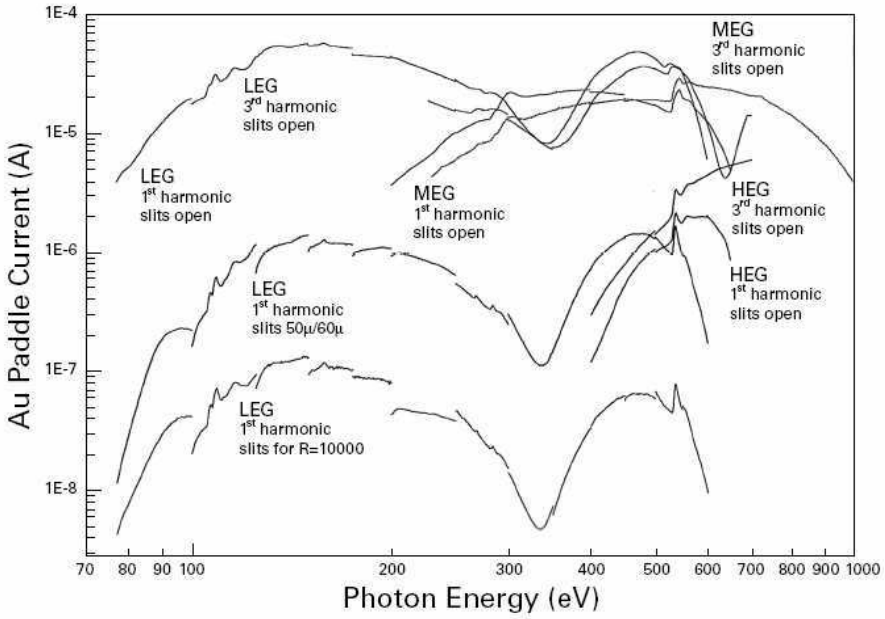

Figure 2.5 Relationship between photon energy and available flux for the three gratings in units of photoelectron current produced from a gold paddle (Figure from ref. 42).

2.6.2.2 The Soft X-ray Fluorescence Endstation

The monochromatic radiation hits the sample placed in the ultrahigh vacuum (UHV) sample chamber and, eventually, the sample emit photons, which are then detected and measured by the soft X-ray fluorescence spectrometer installed in the endstation. This spectrometer consists of a variable entrance slit, a grating chamber containing four interchangeable spherical gratings, and a multichannel plate detector. Figure 2.6, obtained from the ALS website [43] shows a schematic layout of the soft X-ray spectrometer at the BL 8.0.1 at ALS.

Similar to the monochromator, this emission spectrometer also follows the principle of Rowland geometry. In this case, the spectrometer entrance slit, one of four interchangeable diffraction gratings, and the multichannel plate (MCP) detector has to satisfy the Rowland Geometry. The four selectable spherical gratings are employed to cover the whole range of excitation energies supplied by the monochromator.

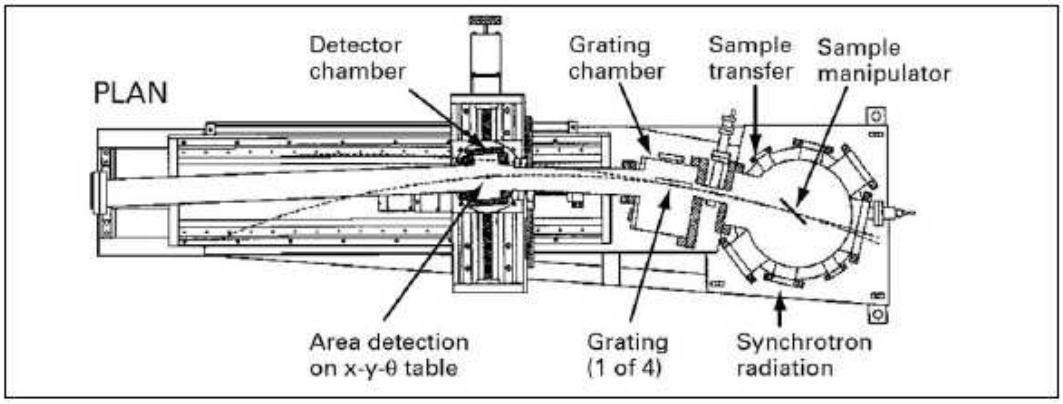

Figure 2.6 Section of the SXF spectrometer at the beamline 8.0.1 at the ALS (Figure from ref. 43).

A sample emits photons equally in all directions and therefore only a very small amount of emitted photon passes through the entrance slit of the spectrometer. In the grating chamber, one of the four gratings is chosen according to the expected energy range of the emission. The diffraction on the grating separates the photons according to their energy by diffracting them at different angles. As a photon strikes on the MCP detector, it will eventually develop an energy dispersed image of the fluorescence radiation. Scanning and data acquisition are automatically done by an IEEE-4888 bus interfaced to a personal computer.

CHAPTER 3
EXPERIMENTAL TECHNIQUES

Reported studies in this thesis are intended to determine the electronic structure of three transition metal oxide systems. Soft X-ray spectroscopy is used as an effective experimental tool in this study. Soft X-ray spectroscopy is a general name for a number of experimental techniques, whereas X-ray absorption spectroscopy (XAS) and X-ray emission spectroscopy (XES) are used in this study. In soft X-ray spectroscopy, photons in the soft X-ray range (approximately 100 eV to 2000 eV) interact with the experimental sample. A spectroscopy experiment involves creation and observation of radiative transitions. When the X-ray beam hits the experimental sample, transitions of core electrons take place to the conduction band (CB) or the continuum. By knowing the energy of the incident X-ray, one can determine the energy separation between the core level and the unoccupied level. This is how XAS probe the local partial densities of unoccupied electronic states. XES detects the emitted photon, which are created when a valence electron refills the core hole created in XAS. The energy of this emitted photon is equivalent to the energy difference between the core level and valence level. This is how XES probe the local partial densities of occupied electronic states. As binding energies are unique, soft X-ray spectroscopy is known as element specific. It is useful to study almost every element of the periodic table as each has binding energies of at least one electron shell within the energy range of soft X-rays. The following sections are intended to describe how these techniques effectively provide information about the electronic structure of systems investigated.

In X-ray spectroscopy, the radiative transitions are governed by the dipole selection rules. These rules determine the possibility of a certain transition to happen. The dipole selection rules for the principal quantum number (n), orbital angular momentum quantum number (ℓ), magnetic quantum number (m_j), spin quantum number (s), and total angular momentum quantum number (j) are listed in Table 3.1. The general notations used to assign the spectroscopic transitions are listed in Table 3.2. Soft X-ray spectra are generally named using the quantum number of the core hole produced through the transition. There are two types of notation as listed in the table. Atomic notations are usually used to describe the transitions in

XAS processes and X-ray notations are common in describing XES processes. Subscripts in X-ray notations are used to denote different sub-shells and subscript increases as the binding energy of the level decreases.

Table 3.1 Dipole selection rules.

Quantum numbers	Constraints
Principal quantum number (n)	not constrained
Orbital angular momentum quantum number (ℓ)	$\Delta\ell = \pm 1$
Spin quantum number (s)	$\Delta s = 0$
Total angular momentum quantum number (j)	$\Delta j = 0$ or ± 1
Magnetic quantum number (m_j)	$\Delta m_j = 0$ or ± 1 (no $m_j = 0 \rightarrow m_j = 0$ if $\Delta j = 0$)

Table 3.2 General notations used in X-ray spectroscopy.

X-ray notation	Atomic notation	Quantum numbers
K	$1s_{1/2}$	$n = 1, \ell = 0, j = 1/2$
L_1	$2s_{1/2}$	$n = 2, \ell = 0, j = 1/2$
$L_{2,3}$	$2p_{1/2,3/2}$	$n = 2, \ell = 1, j = 1/2, 3/2$
M_1	$3s_{1/2}$	$n = 3, \ell = 0, j = 1/2$
$M_{2,3}$	$3p_{1/2,3/2}$	$n = 3, \ell = 1, j = 1/2, 3/2$
$M_{4,5}$	$3d_{3/2,5/2}$	$n = 4, \ell = 1, j = 1/2, 3/2$

3.1 X-ray Absorption Spectroscopy (XAS)

X-ray absorption spectroscopy (XAS) is used as a successful experimental tool to probe the partial density of unoccupied electronic states of a material. In this technique, when the experimental sample is illuminated by synchrotron radiation, transitions of core electrons to the conduction band take place as they absorb energy from the incident radiation. Each element has a characteristic binding energy for a certain core level and therefore XAS is an element specific technique. XAS is also site sensitive and therefore gives information about the bonding environment of the absorbing atom. Thus, XAS provides important information regarding the electronic structure, crystal structure, and chemical information (e.g. oxidation states) of a material, which are directly connected to the various physical properties of the material, for instance, electron transport properties, magnetic properties, and optical properties.

The attenuation of electromagnetic radiation in a material can be described by the Beer's law in expression 3.1.

$$I(x) = I_0 e^{-\mu x} \tag{3.1}$$

Where I_0 is the intensity of the incoming radiation, $I(x)$ is the intensity of the radiation after traversing through the absorbing material, x is the depth of the material that reduces the X-ray intensity to I(x), and μ stands for the attenuation coefficient or absorption coefficient. The absorption co-efficient μ is described by Fermi's golden rule in the one-electron approximation.

$$\mu(\hbar\omega) \propto \sum_f \left|\left\langle \psi_f \left| \vec{p}.\vec{A}(r) \right| \psi_i \right\rangle\right|^2 \delta(E_f - E_i - \hbar\omega) \tag{3.2}$$

In the expression, $\left|\Psi_i\right\rangle$ and $\left|\Psi_f\right\rangle$ represent initial and final states of the transition with energies E_f and E_i, respectively. The notation $\vec{p}$ stands for the momentum operator, and

$\vec{A}(r)$ represents the vector potential of the incident radiation. A valid expression for the absorption cross section can be derived from the above expression.

Figure 3.1 shows a schematic diagram describing the events in XAS processes. In the actual measurement, settings of the undulator gap and monochromator are arranged in such a way that the beamline delivers radiation of the desired energy range to scan over certain absorption threshold. Before falling onto the sample, radiation passes through a gold mesh and photoelectrons are ejected to give rise to a mesh current, which is proportional to the incident radiation and is used to normalize the measured data to the number of incoming photons. When the sample is illuminated by the incoming radiation of desired energy, core electrons of binding energy equal or smaller than the incident energy will be excited and escape from the ground energy state to jump into unoccupied states or to the continuum. Thus the excitation of a core electron leaves a core hole. The resultant core hole can be refilled by either a radiative (X-ray) or a nonradiative (Auger electron; refers to an electron being emitted instead of X-ray) process. Consequently, XAS measurements are accomplished by either measuring the emitted X-rays or by measuring the released electrons. The associated measurement modes are known as Total Fluorescence Yield (TFY for radiative) and Total Electron Yield (TEY for nonradiative). The TFY and TEY detection mode are often used as complementary to each other while both having particular advantages and disadvantages, explained in the sections below. In this thesis, XAS measurement is extensively used to characterize the material employing both of the techniques. Normalized absorption intensity is plotted as a function of the excitation energy in the XAS spectrum. There also exists another method of measuring XAS that is known as transmission mode, in which incoming radiation passes through the material and the intensity of the incoming and outgoing radiation to determine the absorption coefficient is measured as described in equation 3.1. But in the soft X-ray region, transmission mode is not efficient as incoming radiation is less energetic and outgoing radiation is even less energetic. The transmission mode of XAS measurement is popular in hard X-ray absorption spectroscopy.

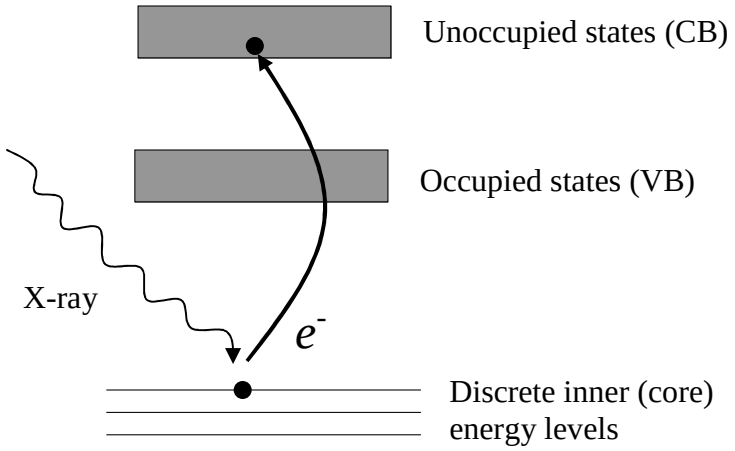

Figure 3.1 Schematic diagram of X-ray absorption spectroscopy.

Figure 3.2 illustrates the different parts of XAS spectra. The XAS spectrum can be divided into four regions: i) pre-edge, ii) X-ray absorption near-edge structure (XANES), iii) near-edge X-ray absorption fine structure (NEXAFS), and iv) extended X-ray absorption fine structure (EXAFS). Pre-edge features are minor and caused by the electronic transitions to empty bound states. These features are sensitive to the local geometry around the absorbing atom and exhibit dependence on the coordination environment (e.g. octahedral, tetrahedral etc.). Absorption edge occurs in the spectrum when the excitation energy reaches the ionization threshold. Edge features show a dependence on the oxidation states and often show an absorption edge shift with increased or decreased oxidation state. NEXAFS occurs when ejected photoelectrons have low kinetic energy and electron scattering cross sections are high. As a consequence, NEXAFS features are dominated by the multiple scattering. In EXAFS, the kinetic energy of photoelectrons is increased and single scattering by the nearest neighbors dominates. Both NEXAFS and EXAFS contain information about the local geometry around the absorbing atom. The latter gives the distances between the various atoms surrounding the excited atom but does not tell anything about the coordination geometry whereas former provides information about the coordination geometry.

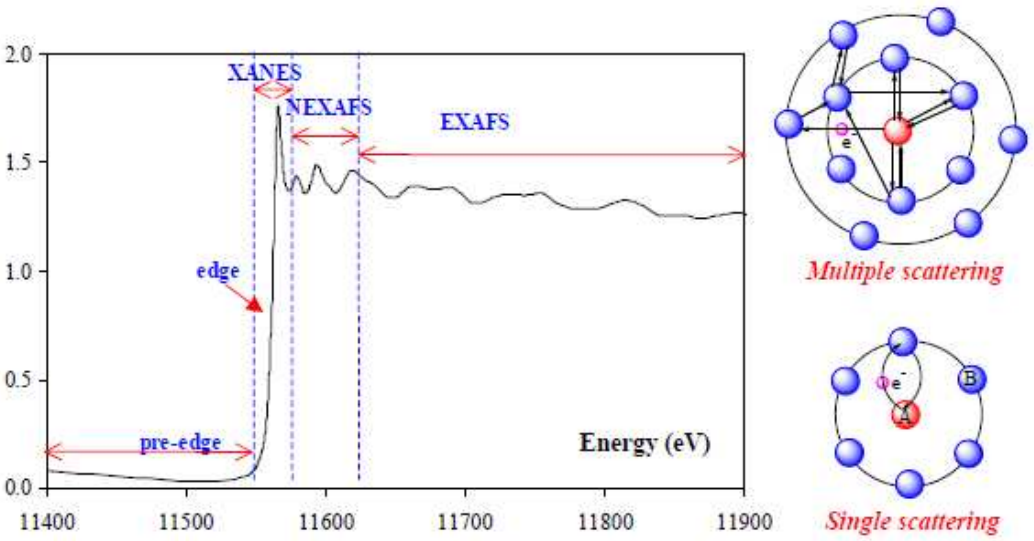

Figure 3.2 Different parts of the XAS spectrum (Figure from ref. 44).

3.1.1 Total Electron Yield (TEY)

Total Electron Yield (TEY) measures the Auger electrons and photoelectrons escaping from the sample. Electrons escaping from the sample would leave a positively charged sample. If the sample is insulated and at ground potential, then electrons will flow from the ground to neutralize the sample and would result in a flow of current. The TEY technique measures that current using a picoammeter to determine the absorption of incoming photons. Higher X-ray absorption would cause more electrons to escape from the sample and therefore generate more sample current. The TEY spectrum displays the normalized intensity of sample current plotted as a function of the excitation energy.

The TEY technique is known to be a surface sensitive technique because it is limited by the mean free path of the electrons. Therefore, electrons situated near the surface (~few nanometers) contribute to generate the sample current. As TEY gives surface sensitive data, it is often desired for a surface sensitive probe in thin films. It also helps identifying differences between surface and bulk electronic structure of a material. For some samples, surface oxidization is a common phenomenon upon air exposure and TEY makes it possible to identify this.

Measurement of XAS using TEY technique is simple but it depends on the conductivity of the sample. If the sample is conductive then the sample current flows easily and gives a well resolved TEY spectrum. But in case of an insulating sample, data will be poor as sample charging may occur. Sample charging occurs when electrons are escaping from the sample but positive charges left behind are not being neutralized by the electrons from the ground, which is because the sample is an insulator and electrons cannot flow. As a result, at some point of time, it will be difficult for the photoelectrons or Auger electrons to escape from the sample and the TEY current will drop drastically.

3.1.2 Total Fluorescence Yield (TFY)

Total fluorescence Yield (TFY) detects and measures the spontaneously emitted photons during the decay of valence electrons to fill core holes created through X-ray absorption. In the TFY measurement, a channeltron placed near the sample inside the UHV sample chamber is used to register some of the emitted photons. Photons emitted from the sample strike on the channeltron plate and cause an electron to emit. A channeltron is an electron multiplier that multiplies incident electrons through a process called secondary emission. In that process, a single electron bombarded on metal, causes emission of 1 to 3 electrons. A high electric potential (~ 3000 V) is applied between this metal plate and another plate placed next to it, which causes electrons to accelerate from the first plate and then to hit the next plate and thus to generate more electrons and so on, until a measurable signal is obtained. Care must be taken not to overload the detector during the measurement. Overloading problems can be minimized by decreasing the potential in the channeltron or by narrowing the slit size to reduce the incoming photons. Finally, normalized fluorescent intensity plotted as a function of the excitation energy constitutes the TFY spectrum.

The TFY technique is known to be bulk sensitive because the mean free path of a photon is considerably longer compared to the mean free path of an electron and therefore, photons can escape from a deeper part of the sample. Combination of both TEY and TFY allows researchers to do comparative studies between the surface and the bulk electronic structure of a sample.

TFY has both advantages and disadvantages. Useful advantages on top of the TEY method are for instance, bulk sensitivity, no possibility of charging effect, etc. One of the limitations is self-absorption, in which emitted photons are being re-absorbed by the sample and thus are not reaching the channeltron. Therefore TFY does not always provide an accurate picture of the total photoabsorption cross-section. Another limitation is that TFY counts emitted photons to provide a measure of absorbed radiation but in reality, Auger process and radiative process compete with each other to refill the core holes and, in some cases, Auger process dominates over the radiative process.

3.2 X-ray Emission Spectroscopy (XES)

X-ray emission spectroscopy (XES) probes the partial density of occupied electronic states of a material. XES involves exciting a core electron to the continuum or to some unoccupied states, and observing the decay from the valence band. Figure 3.3 shows a schematic diagram of the XES process. XES measures the intensity of the emitted radiation as a function of the energy of the emitted radiation using a spectrometer. Similar to XAS, XES is also an element-specific and site-specific technique that makes it a useful tool to study and distinguish different elements. XES is a photon in - photon out process and therefore, no charging effect occurs, which makes this process favorable to measure both conducting and insulating samples. It is a true bulk sensitive technique because the mean free path of a photon is much higher than the mean free path of an electron.

Depending on the excitation energy, XES can be categorized into two different types. One is called Non-resonant X-ray Emission Spectroscopy (NXES), which is used to reveal information about the partial density of occupied states and the other one is called Resonant Inelastic X-ray Scattering (RIXS), which is popular for probing low energy excitations, e.g., *d-d* excitations and charge transfer excitations. These two types of XES are described in the following sections.

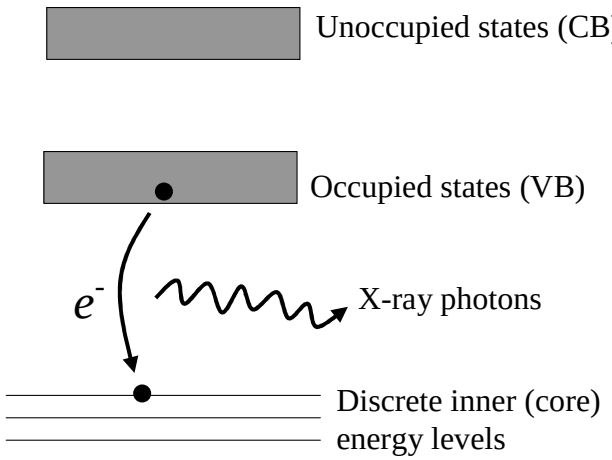

Figure 3.3 Schematic diagram of XES process.

3.2.1 Non-resonant X-ray Emission spectroscopy (NXES)

XAS is the basis for determining excitation energies in emission measurements and, therefore, XAS spectrum is always obtained ahead of measuring a XES. In Non-resonant X-ray Emission spectroscopy (NXES), the excitation energy is chosen well above the ionization threshold of the core state of the element of interest, so that the core electron escapes into the continuum. The resulting core hole gets quickly filled via the fluorescence decay of valence electrons, which is governed by the standard dipole selection rules. Spectral features of an XES spectrum remain unchanged with variation of the excitation energy as long as the excitation energy is chosen well above the absorption threshold. Both NXES and RIXS are second order optical processes where excitation and relaxation process are correlated by the Kramers-Heisenberg formula [45, 46]. By contrast, XAS is a first order process, which only involves a single electron. NXES probes the partial density of the electronic structure of occupied states and, therefore XAS and NXES provide complementary information.

3.2.2 Resonant Inelastic X-ray Scattering (RIXS)

The physical process of Resonant Inelastic X-ray Scattering (RIXS) is different from NXES. For RIXS, excitation energy is just sufficient to resonantly promote an inner electron to a higher unoccupied bound state. To determine the excitation energies for the RIXS measurement, one simply goes over the XAS spectrum of the material looking for the energy position of features. By tuning the excitation energy, RIXS measurements at different XAS

features are obtained. Each individual XAS feature is associated with a particular transition in the material, and therefore the corresponding emission spectrum provides information about the electronic structure of that particular atomic site. A RIXS spectrum can contain both elastic and inelastic features. If the energy position of a certain feature in the RIXS spectrum is the same as the excitation energy, then that feature is recognized as an elastic feature. In contrast, the RIXS features, which track the excitation energy, are due to the inelastic scattering processes. In general, RIXS spectra display elastic features, *d-d* excitation features, and charge transfer features.

The RIXS process is a single inelastic scattering of the incident photon and theoretically described by the Kramer-Heisenberg formula, e.g., 3.3 [45, 46].

$$I(h\nu_{in}, h\nu_{out}) \propto \sum_{f} \left| \sum_{m} \frac{\left\langle f \left| \vec{p}.\vec{A} \right| m \right\rangle \left\langle m \left| \vec{p}.\vec{A} \right| i \right\rangle}{E_m - E_i - h\nu_{in} - i\Gamma/2} \right|^2 .\delta(E_f + h\nu_{out} - E_i - h\nu_{in}) \qquad (3.3)$$

In this expression, $h\nu_{in}$ and $h\nu_{out}$ represents the energies of the incident and emitted photons respectively, $\vec{p}.\vec{A}$ is the dipole operator, $|i\rangle$ is the initial state with energy E_i, $|m\rangle$ is the intermediate state with energy E_m, $|f\rangle$ is the final state with energy E_f, and Γ is the lifetime broadening for the intermediate state. The delta function term is independent of the intermediate state. The radiation damping term $(i\Gamma/2)$ accounts for the resonance, when the other terms in the denominator becomes zero ($h\nu_{in} = E_m - E_i$). The intermediate state in a RIXS measurement is the final state of XAS. As we can see from the expression 3.3, RIXS is a second order optical process consisting of X-ray absorption from $|i\rangle$ to $|m\rangle$ and X-ray emission from $|m\rangle$ to $|f\rangle$.

CHAPTER 4
THEORY AND CALCULATIONS

This chapter is intended to briefly describe the theories used in our calculations, and the software used in analysis accomplished in this thesis. The atomic multiplet theory is explained as it is used throughout the thesis to generate the theoretical spectra. A short description of the Hartree-Fock approximation is provided as it is exploited in atomic multiplet theory. Principal component analysis is introduced in this chapter as it is used as a data analysis tool in some aspects of the present study.

4.1 Hartree–Fock Theory

Hartree-Fock (HF) theory is one of the fundamental electronic structure theories. A step-by-step derivation of the HF equation is presented by C. David Sherril in ref. 47. The very brief description presented in this section is adapted from that work. HF theory assumes that the motion of each electron in a system can be described by a single-particle wave function, i.e., no correlations to the instantaneous motion of other electrons of the system are taken into account. It is a good approximation to the actual wave function and thus considered as a useful starting point for more precise calculations. The solution to the electronic problem of the hydrogen atom is known analytically. If we consider adding one more electron to the hydrogen atom and assume no interaction between two electrons, then the total electronic wave function describing the motion of two electrons can be written as a product of the individual wavefunction of the two electrons, which is known as the Hartree product.

$$\Psi(r_1, r_2) = \Psi_H(r_1)\Psi_H(r_2) \tag{4.1}$$

Therefore, for an N-electron system, the Hartree product can be extended as follows.

$$\Psi_H(r_1, r_2, ..., r_N) = \phi(r_1)\phi(r_2)...\phi_N(r_N) \tag{4.2}$$

Now, introducing the space-spin coordinates (as electrons also possess spin coordinates), a more appropriate form of the Hartree product can be written by changing the notation from $\phi(r)$ to $\chi(x)$.

$$\Psi_H(x_1, x_2, ..., x_N) = \chi_1(x_1)\chi_2(x_2)...\chi_N(x_N) \tag{4.3}$$

In the above expression x is a function of space and spin coordinates, i.e., $x = \{r, \omega\}$. The variable ω represents the spin coordinate, and consequently $\chi(x)$ represents a spin orbital function instead of $\phi(r)$ that only represents a spatial orbital function. But this wave function does not satisfy the antisymmetry principle, which states that a wave function describing fermions should be antisymmetric under the interchange of space-spin coordinates. To solve this problem, a wave function in the form of a determinant of spin orbitals is introduced (details can be found in ref. 47), which is called a *Slater determinant* named after John Slater.

$$\Psi = \frac{1}{\sqrt{N!}} \begin{vmatrix} \chi_1(x_1) & \chi_2(x_1) & . & . & . & \chi_N(x_1) \\ \chi_1(x_2) & \chi_2(x_2) & . & . & . & \chi_N(x_2) \\ . & . & . & & & . \\ . & . & & . & & . \\ . & . & & & . & . \\ \chi_1(x_N) & \chi_2(x_N) & . & . & . & \chi_N(x_N) \end{vmatrix} \tag{4.4}$$

In the expression, N represents the total number of electrons. Now, this functional form remains antisymmetric under any interchange of space-spin coordinates and satisfies the Pauli Exclusion Principle.

To determine the energy of molecular orbitals, one can use the usual quantum mechanical expression given by the following expression.

$$E_{el} = \langle \Psi | H_{el} | \Psi \rangle \tag{4.5}$$

Where Ψ is the HF wavefunction and H_{el} represents the typical *Hamiltonian* given by

$$H_{el} = \sum_{i=1}^{N} h(i) + \sum_{i<j}^{N} V_{\text{int}}(i, j) \tag{4.6}$$

Where $h(i)$ is the single-particle Hamiltonian for the particle-i and $V_{\text{int}}(i, j)$ describes the interaction between the electrons i and j. For an N-electron system with atomic number Z, one can write,

$$h(i) = \frac{\vec{p}_i^{\,2}}{2m} - \frac{Ze^2}{r_i} \tag{4.7}$$

$$V_{\text{int}}(i, j) = \frac{e^2}{\left|\vec{r}_i - \vec{r}_j\right|} \tag{4.8}$$

Note that the Hamiltonian does not consider any external fields, relativistic effects, and spin-dependent terms. One can rewrite the Hartree-Fock energy E_{el} in terms of integrals of the one- and two-electron operators as stated in the following equation.

$$E_{HF} = \sum_i \langle i|h|i\rangle + \frac{1}{2}\sum_{ij} \left[ii|jj\right] - \left[ij|ji\right] \tag{4.9}$$

Where the one-electron integral is given by

$$\langle i|h|j\rangle = \int dx_1 \chi_i^{*}(x_1) h(r_1) \chi_j(x_1) \tag{4.10}$$

and a two-electron integral is given by the following expression.

$$\left[ij|kl\right] = \int dx_1 dx_2 \chi_i^{*}(x_1) \chi_j(x_1) \frac{1}{r_{12}} \chi_k^{*}(x_2) \chi_l(x_2) \tag{4.11}$$

Efficient computer program exists that are used to calculate these integrals. To determine the HF equation, the variational method is applied, i.e., the HF energy expression is minimized with respect to changes in the orbitals $\chi_i \to \chi_i + \delta\chi_i$. The HF energy formula given in equation 4.9 is valid only if orbitals χ are orthonormal. Therefore the energy expectation values should be varied under the constraint that the variational method leaves the orbitals orthonormal. This is obtained by using the Lagrangean multipliers method. Working through the variational method using Lagrange's method of undetermined multipliers, one can derive the HF equations defining the orbitals as follows.

$$h(x_1)\chi_i(x_1) + \sum_{j\neq i}[\int dx_2 \left|\chi_j(x_2)\right|^2 r_{12}^{-1}]\chi_i(x_1) - \sum_{j\neq i}[\int dx_2 \chi_j^*(x_2)\chi_i(x_2) r_{12}^{-1}]\chi_j(x_1) = \varepsilon_i \chi_i(x_1)$$

$$\Rightarrow \left[h(x_1) + \sum_{j\neq i} \Im_j(x_1) - \sum_{j\neq i} \kappa_j(x_1) \right] \chi_i(x_1) = \varepsilon_i \chi_i(x_1) \qquad (4.12)$$

Where ε_i is the energy eigenvalues associated with orbital χ_i. This is the well-known HF equation. The term $\Im_j(x_1)$ is called the *Coulomb operator*, which gives the Coulomb interaction of an electron with spin orbital χ_i with the average charge distribution of the other electrons. The other term $\kappa_j(x_1)$ arises from the antisymmetry requirement of the wave functions, and is called *exchange operator*. The Coulomb and exchange operators are expressed as

$$\Im_j(x_1) = \int dx_2 \left|\chi_j(x_2)\right|^2 r_{12}^{-1} \qquad (4.13)$$

and $$\kappa_j(x_1)\chi_i(x_1) = [\int dx_2 \chi_j^*(x_2) r_{12}^{-1} \chi_i(x_2)]\chi_i(x_1) \qquad (4.14)$$

Now, let us introduce a new operator called *Fock operator* defined by the following expression.

$$f(x_1) = h(x_1) + \sum_j \Im_j(x_1) - \kappa_j(x_1) \tag{4.15}$$

A more compact form of the HF equation can be written as

$$f(x_1)\chi_i(x_1) = \varepsilon_i \chi_i(x_1) \tag{4.16}$$

It has the form of an eigenvalue equation similar to the N-electron Schrödinger equation. An iterative method is necessary to solve the equation because Coulomb and exchange operators are determined by the orbitals χ_i, which are yet to be determined by solving the HF equation 4.16. One starts with a guess $\chi_i(0)$ that constructs the Fock operator $f(0)$ and solves the HF equation. The obtained solution for the orbital and orbital energies are then used to construct a new Fock operator $f(1)$, which is further used to solve the HF equation. This process of iteration is repeated until the initial orbitals used for constructing Fock operator are found identical to the solution obtained from the HF equation. The HF method is also known as the "self-consistent field" (SCF) method due to this "self-consistency". The application of HF theory is limited because it does not take the interaction with neighboring electrons into account. However, it is useful to effectively model the molecular orbitals of various systems.

4.2 Atomic Multiplet Theory

Atomic multiplet theory was first developed to study the core level photoemission spectra [48-51], which was later improved by Asada *et al*. by the inclusion of charge transfer theory [52]. The theory was then further extended by B. T. Thole to include crystal field effects. In 1985, B. T. Thole calculated all $3d^{10}\,4f^{\,N} \rightarrow 3d^{9}\,4f^{\,N+1}$ transitions [53] using Cowan's atomic HF program [54, 55]. Comparison of his calculation with the experimental spectra confirmed the correctness of the theory [53]. Atomic multiplet theory was successfully used to simulate the spectra of manganese impurities in noble metals by calculating the $2p^6\ 3d^5 \rightarrow 2p^5\ 3d^6$ transition [56].

4.2.1 The Origin of Atomic Multiplets

In XAS, a core electron is excited to an empty state generating a core hole, for instance, a 2*p* core hole is created in Mn 2*p* XAS transition, $2p^6\ 3d^5 \rightarrow 2p^5\ 3d^6$. Thus the final state of X-ray absorption process contains a partly filled core state ($2p^5$) and also a partly filled 3*d*-band ($3d^6$). A strong overlap between 2*p*-hole and 3*d*-hole radial wave functions split the XAS final states. Those can be obtained by the vector coupling of 2*p* and 3*d* wave functions [57]. These XAS final states created through splitting are known as atomic multiplets. The overlapping of wave functions also exists in the ground state, but does not play an effective role as the core states in XAS ground state are filled [57]. The atomic multiplet effects are also observed in solids and it was experimentally found that it plays similar role (of the same order of magnitude) in both the solids and the atoms [57]. This is why the common single particle code is not capable of calculating correct density-of-states for XAS of a transition metal $L_{2,3}$ edges. Calculated XAS in transition metal *K*-edges and O *K*-edges using single particle codes are found in nice agreement with the experiment as multiplet effects are considerably reduced for 1*s*-core hole due to screening effect. Details of the description of the origin of atomic multiplets can be found elsewhere [57].

4.2.2 Treatment of XAS using Atomic Multiplet Theory

The X-ray absorption cross-section obtained from the Fermi's golden rule can be expressed by the following expression.

$$\sigma(E_X) \sim \sum_f \left| \langle \phi_i | X | \phi_f \rangle \right|^2 \delta(E_i + E_X - E_f) \tag{4.17}$$

In the expression E_X, E_i, and E_f represent the incident X-ray energy, the energy of the initial state, and the energy of the final state, respectively. The initial and final state wave functions are denoted by ϕ_i and ϕ_f. X represents the perturbation acting on the system, which is absorption of photons during XAS. In the expression, ϕ_i and ϕ_f are coupled through the aforementioned dipole selection rules. For Mn 2*p* XAS, the allowed dipole transitions are $2p \rightarrow 3d$, and $2p \rightarrow 4s$, but the $2p \rightarrow 4s$ transition is negligible with respect to $2p \rightarrow 3d$. Atomic multiplet theory assumes that, for a transition metal compound, the 2*p*-3*d* and also the

3*d*-3*d* coupling effects are very important to consider in the treatment of transition metal $L_{2,3}$ XAS, whereas single-particle theory does not take these couplings into account. In atomic multiplet code, multiplets are initially calculated neglecting the solid-state effect, which is later added to the Hamiltonian by introducing a crystal field parameter, treated as a free parameter to be varied to obtain good agreement with the experiment. Therefore, from the atomic standpoint, the expression for the absorption cross-section in 3*d*-transition metal 2*p* XAS can be written as follows [58].

$$\sigma_{2p}(E_X) \sim \sum_j \left| \left\langle \phi_G (3d^N)_{O(3)} \middle| X \middle| \phi_{fi} (2p^5 3d^{N+1})_{O(3)} \right\rangle \right|^2 \delta(E_G + E_X - E_f) \tag{4.18}$$

In the expression, $\phi_G (3d^N)_{O(3)}$ represents the ground state in spherical symmetry $O(3)$ and $\phi_{fi} (2p^5 3d^{N+1})_{O(3)}$ represents the *j*-th final state in the atomic multiplet spectrum in spherical symmetry $O(3)$.

4.2.3 The Form of the Hamiltonian

Let us start considering a free atom without any influence from the surroundings. The Hamiltonian for an *N*-electron atom can be written in the form stated as follows.

$$H = \sum_N \frac{p_i^2}{2m} + \sum_N \frac{-Ze^2}{r_i} + \sum_{pairs} \frac{e^2}{r_{ij}} + \sum_N \zeta(r_i) l_i \cdot s_i \tag{4.19}$$

In the expression, the first term represents the kinetic energy of electrons, the second term represents the electrostatic interaction of electrons with the nucleus, the third term represents the electron-electron repulsion (H_{ee}), and the last term stands for the spin-orbit coupling ($H_{\ell s}$) of each electron. In a given atomic configuration, the first two terms in the Hamiltonian define the average energy of the configuration (H_{avg}) and do not contribute to the multiplet splitting. The remaining two terms define the relative energy of the different terms within the configuration and contribute to the multiplet splitting. The electron-electron repulsion term (H_{ee}) is too large to be considered as a perturbation and creates difficulty in solving the

Schrödinger equation. However, using the central field approximation, spherical average ($\langle H_{ee} \rangle$) is separated from the non-spherical part of the electron-electron interaction and the spherical average $\langle H_{ee} \rangle$ is added to H_{avg} to form the average energy. Then the effective electron-electron interaction H'_{ee} is expressed as follows.

$$H'_{ee} = H_{ee} - \langle H_{ee} \rangle = \sum_{pairs} \frac{e^2}{r_{ij}} - \left\langle \sum_{pairs} \frac{e^2}{r_{ij}} \right\rangle \tag{4.20}$$

Therefore, the effective electron-electron interaction H'_{ee} plus the spin-orbit coupling $H_{\ell s}$ defines the effective Hamiltonian responsible for the multiplet splitting that determines the energy of the different terms in the configuration. The following section describes the definition of different term symbols often used in atomic multiplet theory.

4.2.4 Definition and Notation of Term Symbols

Term symbols allow someone to find out the three relevant quantum numbers as well as to determine the energy and symmetry associated with a certain configuration. Considering the usual definition of quantum numbers (orbital moment *L*, spin moment *S*, and total moment *J*), the so-called term symbols are defined as ${}^{2S+1}X_J$, where *X* represents the orbitals *S*, *P*, *D*… etc. corresponding to the orbital moment of L = 0 , 1, 2… etc. If we neglect the spin-orbit coupling effect, all the configurations having same *L* and *S* value are of the same energy with (2*L* + 1) (2*S* + 1)-fold degenerate energy levels. In necessary cases, when spin-orbit coupling is considered, all terms are split in energy in accordance with their *J*-value giving (2*J* + 1)-fold degenerate energy levels with $|L-S| \le J \le |L+S|$. To give some examples, for a 1*s* electron (*L* = 0, *S* = 1/2, and *J* = 1/2), the term symbol is written as ${}^2S_{1/2}$ and similarly, for a 2*p* electron (*L* = 1, *S* = 1/2, and *J* = 1/2, 3/2), the term symbols are ${}^2P_{1/2}$ and ${}^2P_{3/2}$, as spin-orbit coupling is important in this case. These two terms are seen in the experimental metal 2*p* XAS of transition metal as L_2- and L_3-peaks. Now, going into a little complex configuration, for example $3d^1 4d^1$, the term symbols are obtained through the multiplication of the individual term symbols of 3*d* and 4*d* electrons, i.e., by calculating, ${}^2D \otimes {}^2D$. The product

$^2D \otimes {}^2D$ gives, L = 0, 1, 2, 3, or 4 and S = 0 or 1, thus one can obtain 10 LS term symbols represented by ^1S, ^1P, ^1D, ^1F, ^1G, ^3S, ^3P, ^3D, ^3F, and ^3G with a total degeneracy of 100 as listed in table 4.1 adapted from the ref. 59. Inclusion of spin-orbit coupling gives a total of 18 term symbols.

Table 4.1 Total degeneracy of $3d^1 4d^1$ configuration [59].

$3d^1 4d^1$	^1S	^1P	^1D	^1F	^1G	^3S	^3P	^3D	^3F	^3G	$\sum$
Degeneracy	1	3	5	7	9	3	9 0	15 1	21 2	27 3	100
J-values	0	1	2	3	4	1	1 2	2 3	3 4	4 5	

In case of a $3d^2$ configuration, the Pauli exclusion principle does not allow two 3*d*-electrons to occupy the same quantum state, suggesting the possibility of 45 (= 10 × 9/2) combinations [59]. For a $3d^3$ configuration it can be shown that 120 (= 10 × 9/2 × 8/3) combinations are possible [59]. The general expression for determining the degeneracy of a $3d^N$ configuration is expressed as follows [59].

$$\binom{10}{n} = \frac{10!}{(10-n)!n!} \tag{4.21}$$

4.2.5 Determination of the Relative Energies of Different Terms

To determine the relative energies of different terms derived from the formula $^{2S+1}X_J$, one calculates the matrix elements of these states with the effective Hamiltonian defined in the aforementioned expression (4.20). The general formula to calculate the matrix elements is obtained as follows [59].

$$\left\langle {}^{2S+1}L_J \left| \frac{e^2}{r_{12}} \right| {}^{2S+1}L_J \right\rangle = \sum_k f_k F^K + \sum_k g_k G^k \tag{4.22}$$

In the expression, F^K and G^K are the so-called Slater-Condon parameters. The Coulomb repulsion terms are denoted by F^K and the exchange terms are denoted by G^K. The Wigner-Eckardt theorem is used to separate the radial parts F^K and G^K in the above expression and Legendre polynomials are used to expand the Hamiltonian $1/r_{12}$ in a series [60]. The angular coefficients f_K and g_K are calculated using the angular momentum coupling and results are expressed in terms of 3*j* and 6*j* symbols as follows [59].

$$f_K = (2l_1+1)(2l_2+1).(-1)^L \begin{pmatrix} l_1 & k & l_1 \\ 0 & 0 & 0 \end{pmatrix} \begin{pmatrix} l_2 & k & l_2 \\ 0 & 0 & 0 \end{pmatrix} \begin{Bmatrix} l_1 & l_2 & L \\ l_2 & l_1 & k \end{Bmatrix} \tag{4.23}$$

$$g_K = (2l_1+1)(2l_2+1).(-1)^S \begin{pmatrix} l_1 & k & l_2 \\ 0 & 0 & 0 \end{pmatrix} \begin{pmatrix} l_1 & k & l_2 \\ 0 & 0 & 0 \end{pmatrix} \begin{Bmatrix} l_1 & l_2 & L \\ l_2 & l_1 & k \end{Bmatrix} \tag{4.24}$$

The exchange interaction g_K does not exist for equivalent electrons, and f_K is simplified using $l = l_1 = l_2$. The values of k are calculated using the triangle conditions of 3*j*-symbols. Calculating 3*j* symbols of equation 4.23 and 4.24, one can find that for f_K: i) k must be even, ii) $k = 0$ always exists, and iii) the maximum value of k is twice of the lowest value of l [59]. Also, for g_K: i) k is even if $l_1 + l_2$ is even, ii) k is odd if $l_1 + l_2$ is odd, and iii) the maximum value of k is $l_1 + l_2$ [59]. Table 4.2 adapted from the ref. 59 summarizes k-values for some commonly used configurations.

Table 4.2 List of k-values, corresponding to the angular coefficient f_K and g_K [59].

Config.	f_K	g_K	Config.	f_K	g_K	Config.	f_K	g_K
$1s^2$	0		1*s*2*s*	0	0	1*s*2*p*	0	1
$2p^2$	0 2		2*p*3*p*	0 2	0 2	2*p*3*d*	0 2	1 3
$3d^2$	0 2 4		3*d*4*d*	0 2 4	0 2 4	3*d*4*f*	0 2 4	1 3 5

For a $3d^2$ configuration, there will be 5 term symbols, ${}^1S$, ${}^3P$, ${}^1D$, ${}^3F$, and ${}^1G$. The exchange interaction g_K does not exist for a $3d^2$ configuration as electrons are from the same shell. The k-values for f_K are 0, 2, and 4. The angular coefficient f_0 is equal to the number of permutations (N (N-1)/2) of N electrons (i.e., $f_0 = 1$ for $3d^2$ configuration). The remaining coefficients f_2 and f_4 can be found from the following expression [59].

$$f_h = \frac{10}{7}\begin{pmatrix} 2 & 2 & L \\ 2 & 2 & k \end{pmatrix}(-1)^L \tag{4.25}$$

Energies of the five term symbols for $3d^2$ configuration can be calculated assuming that in case of a 3d-transition metal the Slater-Condon parameters $F^K = 10$ eV, and F^4 and F^2 show an approximate ratio of $F^4 = 0.62\,F^2$. One finds that ${}^3F$ is at -1.8 eV, ${}^1D$ is at -0.1 eV, ${}^3P$ is at +0.2 eV, ${}^1G$ is at +0.8 eV, and ${}^1S$ is at +4.6 eV. Details of the calculation can be found in ref. 59. The ${}^3F$ term is at lowest energy and therefore represents the ground state of the $3d^2$ configuration satisfying the Hund's rule. The terms ${}^1D$, ${}^3P$, and ${}^1G$ fall in the energy region of 1.7 - 2.5 eV above the ground state. The state ${}^1S$ is situated at 6.4 eV above the ground state as two electrons in the same orbital strongly repel each other.

In case of three or more electron systems, the situation is more complex because writing an antisymmetrized three-electron wave function is not so simple. In that case, using the so-called coefficients of fractional percentage theory, the three-electron wave function is generated from a series of two-electron wave functions.

4.2.6 Inclusion of the Crystal Field

So far we have considered a free atom, which is an ideal but rare case. To actually calculate an XAS spectrum showing good agreement with the experiment, it is necessary to include solid state effects. Crystal field theory was incorporated into atomic multiplet theory by Thole and his co-workers [53]. Atomic multiplet theory is extended by adding a new term in the atomic Hamiltonian representing an electrostatic field. This new term contains electronic charge e times a potential ϕ (r) representing the solid state effect. The crystal field is

considered as a perturbation to the atomic case and one should determine the matrix elements of ϕ(r) with respect to the 3*d*-orbitals $\langle 3d|\phi(r)|3d\rangle$. Simulation of an XAS spectrum consists of a calculation of atomic matrix elements for the initial state, final state, and the transition. To include the crystal field effect, the atomic matrix element should be branched to cubic symmetry. For simplicity, the following discussion about the effect of inclusion of a crystal field is limited only to an octahedral crystal field.

In octahedral symmetry, a transition metal is surrounded by six neighboring atoms situated on the three Cartesian axes. The introduction of an octahedral field causes reduction of symmetry from spherical $O(3)$ to O_h. The group theoretical discussion regarding the $O(3)$ to O_h transformation is described in refs. 61-63. When an octahedral crystal field is introduced, 5-fold degenerate 3*d*-orbitals become grouped into two categories represented by E_g and T_{2g} symmetry. The state E_g contain the orbitals that are pointing towards the ligand ($d_{x^2-y^2}$ and d_{z^2}) and, as a consequence, they experience strong electrostatic repulsion. The state T_{2g} contain orbitals which are pointing between the ligands (d_{xy}, d_{yz}, and d_{zx}) and therefore, experience considerably less repulsion. The general result of this splitting is listed below in Table 4.3 adapted from the Tanabe-Sugano diagrams [64]. The effect of cubic crystal field on the energies of atomic states is presented in Tanabe-Sugano diagram [64] shown in the following Figure 4.1 adapted from ref. [64].

The crystal field multiplets are calculated using the method outlined above and compared with the experiment. In the calculation, the atomic Hamiltonian is solved using a HF approximation, which assumes that the ground state can be represented by a single $3d^N$ configuration. This assumption is erroneous because the ground state is not a single configuration but consists of a mixture of configurations. As an approach to correct this, all the Coulomb and exchange parameters (Slater integrals) are reduced to 80% of the HF-values to account for the intra-atomic interactions. Crystal field parameters are treated as a free parameter to be varied to obtain good agreement with the experiment. To compare with the experiment, our calculated line spectra are broadened with Lorentzian and Gaussian

broadening to account for the life-time effects and the resolution function of the instrument, respectively.

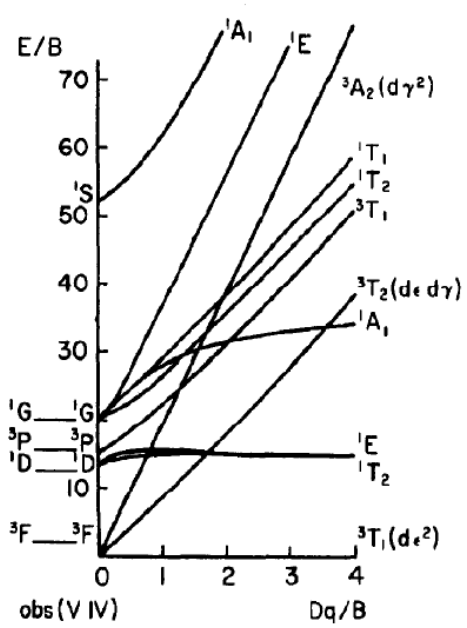

Figure 4.1 Tanabe-Sugano diagram for the ground state of $3d^2$ configuration in cubic symmetry (Figure from ref. 64).

Table 4.3 Branching in an octahedral field.

Term	Degeneracy	States in octahedral field
S	1	A_{1g}
P	3	T_{1g}
D	5	$E_g + T_{2g}$
F	7	$A_{2g} + T_{1g} + T_{2g}$
G	9	$A_{1g} + T_{1g} + T_{2g} + E_g$
H	11	$T_{1g} + T_{1g} + T_{2g} + E_g$
I	13	$A_{1g} + A_{2g} + T_{1g} + T_{1g} + T_{2g} + E_g$

Two separate program sets are used in this thesis to perform atomic multiplet calculations. One is called Basis state edition (BSE), which does not include crystal fields and the other one is called Crystal Field Atomic Multiplet Calculation that include crystal fields. The program BSE is written by R. D. Cowan [54], and the Crystal Field Atomic Multiplet program used in this thesis is a slightly modified version of the one written by B. T. Thole [53, 56], where the modifications are added by Jason Sadowski, Mark Hlady, and Adrian Hunt at the University of Saskatchewan.

4.3 Principal Component Analysis (PCA)

Principal Component Analysis (PCA) is a very useful data decomposition tool. It is a simple one and takes a little effort to extract valuable information about the system. It helps identifying the constituents in a dataset by reducing a complex data set to a lower dimension. PCA is used in chemistry to analyze the spectral data of systems containing a mixture of chemical compounds. Also, PCA is successfully used to analyze the XAS spectra of different samples exhibiting changes in structure or composition [65-69]. PCA provides a systematic approach to separate a spectral mixture into independent components and thus to extract information regarding the constituents of the data set. PCA determines the minimum number of component spectra necessary to reconstruct an experimental spectrum. These components are mathematical constructs and do not have any physical meaning but comparison of these component spectra with experimental reference spectra yields information about the composition of the sample. This information can be verified afterward by constructing a fit for the experimental spectrum using a weighted linear combination of the reference spectra. The associated weighting factor quantifies the importance of the presence of each individual reference spectrum in the experimental sample.

If there are p components (x_1, x_2, …, x_p) in a dataset, PCA forms different combinations of the components to reduce the number of variables giving uncorrelated principal components $PC_{(1)}$, $PC_{(2)}$, …, $PC_{(p)}$, known as eigenvectors. The program gives a list of obtained eigenvectors in an ordered arrangement so that variance ($PC_{(1)}$) ≥ variance ($PC_{(2)}$) ≥ … ≥ variance ($PC_{(p)}$), where variance of a certain component represents the eigenvalues of that component. Usually, some eigenvectors obtained through PCA are found to show negligible

eigenvalues indicating that these are not necessary to reconstruct the dataset. The program allows users to check the necessity of each individual eigenvectors in reconstructing the original dataset and thus checking one by one, the minimum number of eigenvectors is determined. This is how PCA reduces the number of variables in a dataset. Again, these eigenvectors are mathematical entities and do not bear any physical meaning. Therefore, the spectra of eigenvectors are compared with the known experimental data of different reference compounds to determine what physical components are present in the dataset. The mathematical details of the PCA method are explained elsewhere [70].

In this thesis, PCA is performed using the '*Exafspak*' software [71] to determine the presence of different Mn-valence states in $La_{1-x}Ca_xMnO_3$ (x = 0.20, 0.21, 0.23, and 0.25) samples. The input to the PCA routine is the set of $La_{1-x}Ca_xMnO_3$ measured data taken at Mn 2*p* edges, and the output is a series of eigenvectors that are needed to reconstruct each spectrum in the data set. By systematically testing whether an eigenvector is necessary for reconstruction, the minimum number of components in the data set is determined. Then 'target transformation' in the software suite is used to determine if a particular Mn-valence (Mn^{2+} and/or Mn^{3+}) is present in the $La_{1-x}Ca_xMnO_3$ data set. Experimental XAS data of MnO and Mn_2O_3 are used as experimental reference spectra for Mn^{2+} and Mn^{3+} in the target transformation.

CHAPTER 5
RESULTS AND DISCUSSION

5.1 Electronic structure of Ca-doped $LaMnO_3$

An investigation of the Ca-doped $LaMnO_3$ single crystals using a combination of XAS measurements and atomic multiplet calculations is reported to study the valence of manganese sites. Mn 2*p* and O 1*s* XAS spectra of $La_{1-x}Ca_xMnO_3$ (x = 0.20, 0.21, 0.23, 0.25) single crystals measured TEY and TFY mode are presented. $La_{1-x}Ca_xMnO_3$ single crystals are grown using the floating zone (FZ) melting method [72]. Details of the growth technique and conditions are described elsewhere [73]. X-ray powder diffraction measurements confirmed that the sintered materials are single-phased [73]. The magnetic and charge transport properties of these single crystals are also reported elsewhere [74]. In this study, Mn 2*p* and O 1*s* XAS spectra of $La_{1-x}Ca_xMnO_3$ samples and associated reference samples $LaMnO_3$ (Mn^{3+}), MnO (Mn^{2+}), Mn_2O_3 (Mn^{3+}), and Mn_3O_4 (Mn^{2+} + Mn^{3+}) are measured at the undulator-based SGM beamline at the CLS. Mn $L_{\alpha,\beta}$ RIXS measurements of $La_{1-x}Ca_xMnO_3$ are performed at beamline 8.0.1 at the ALS. In XAS TEY measurement, absorption is monitored via the measurement of the sample current, whereas TFY is monitored through the detection of photons produced during the relaxation of excited states. For XAS data of post-annealed $La_{1-x}Ca_xMnO_3$, the samples were annealed at 1000 °C in air for 2 hours and were measured as soon as possible (~10 minutes) to avoid longer air exposure. The estimated experimental energy resolution is 0.1 eV for the series of measurements. All spectra are recorded at room temperature and are normalized to the number of photons falling on the sample monitored by a highly transparent gold mesh. Note that, the phrase 'mixture of Mn^{2+} and Mn^{3+} (Mn^{2+} + Mn^{3+})' is used in this report to represent just a mixture without any interaction between two oxidation states.

The PCA is performed using the '*Exafspak*' software [71] to determine the presence of different Mn-valence states in $La_{1-x}Ca_xMnO_3$ samples. The experimental Mn 2*p* XAS spectra of MnO (Mn^{2+}), Mn_2O_3 (Mn^{3+}), and Mn_3O_4 (Mn^{2+} + Mn^{3+}) are simulated using the program called Crystal field atomic multiplet calculation (Appendix A) by calculating the transitions $2p^63d^n \rightarrow 2p^53d^{n+1}$. Since Mn ions are octahedrally coordinated in MnO and Mn_2O_3 [16], an

octahedral crystal field of 0.9 eV and 1.1 eV are chosen to calculate the XAS spectra of Mn^{2+} and Mn^{3+}, respectively. These values of crystal field are in close agreement with the refs. 58 and 75**.** XAS spectrum of Mn^{2+} + Mn^{3+} is calculated using the superposition of individually calculated Mn^{2+} and Mn^{3+}. Relative weights of 30% (± 5%) of Mn^{2+} and 70% (± 5%) of Mn^{3+} are used in the superposition. Multiplet coupling parameters such as the Slater integrals for the $3d^n$ states are reduced to 80% to account for intra-atomic relaxation effects [76]. The calculated line spectra are broadened with the Gaussian broadening of 0.5 eV and 0.7 eV for Mn^{2+} and Mn^{3+}, respectively. We will see in Figure 5.2 that the theoretical simulation reproduces the main features of the experimental spectra reasonably well. The differences can be attributed to the contribution from the covalency of the compound as *d*-count can reach a non-integer value for the covalent compounds and as a consequence, assumed transition $2p^6 3d^n \rightarrow 2p^5 3d^{n+1}$ is no longer valid [76]. Another reason for the difference could be some deviation from the octahedral symmetry caused by the oxygen vacancies [77].

5.1.1 XAS Data Analysis

Mn 2*p* XAS. Figure 5.1 shows Mn 2*p* XAS TEY spectra of $La_{1-x}Ca_xMnO_3$ single crystals. The detection depth of TEY measurements is governed by the escape depth of the photoelectrons and for this particular case it is approximately 4 to 5 nm [78]. All spectra are normalized to the intensity of the first sharp feature located at ~ 640.8 eV. Due to the spin-orbit splitting of the 2*p* core level, $2p \rightarrow d$-symmetry transitions give rise to two edges, namely $2p_{3/2}$ (L_3-edge) and $2p_{1/2}$ (L_2-edge) separated by ~11 eV. Due to the large number of unoccupied conduction band (CB) *d*-states, each edge has sharp peaks (white lines). The intensity of the L_3-peak is expected to be higher compared to the L_2-peak because of the higher number of electrons available at $2p_{3/2}$ compared to $2p_{1/2}$. Previous studies of Mn 2*p* XAS in oxides have shown that the energy position of spectral features are very sensitive to the oxidation state of Mn atoms and can be used to determine the Mn-valency [18-21]. The double-peak feature of the L_3-edge changes as the Ca-concentration increases. The peak at approximately 640.8 eV shows highest relative intensity for the $x = 0.20$ sample and then the intensity decreases with increasing Ca-concentration. Conversely, the relative intensity of the peak at approximately 642.3 eV increases with increasing Ca-concentration. To characterize the features, PCA and atomic multiplet calculations are used to analyze the data. The PCA of the $La_{1-x}Ca_xMnO_3$

data set using the model spectra of experimental Mn^{2+} and Mn^{3+} suggests that Mn^{2+} and Mn^{3+} are present at the surface of $La_{1-x}Ca_xMnO_3$ (x = 0.20, 0.21, 0.23, and 0.25) surfaces. An atomic multiplet calculation is presented in the following paragraph to confirm the presence of Mn^{2+} and Mn^{3+}.

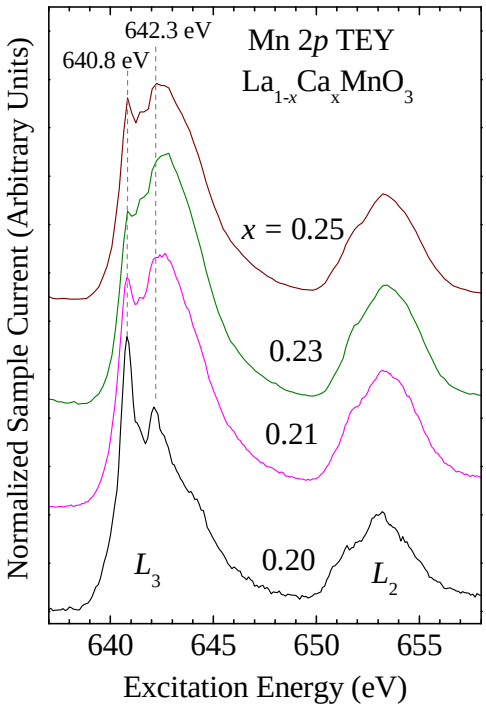

Figure 5.1 Mn 2*p* XAS TEY spectra of $La_{1-x}Ca_xMnO_3$ samples. Dashed vertical lines are drawn to level the energy position of the spectral features. Two vertical lines at 640.8 eV and 642.3 eV are drawn to show characteristic peaks for Mn^{2+} and Mn^{3+}, respectively.

Figure 5.2 shows the comparison between experimental and atomic multiplet calculation of Mn 2*p* XAS spectra of MnO (Mn^{2+}), Mn_2O_3 (Mn^{3+}), and Mn_3O_4 (Mn^{2+} + Mn^{3+}), which are used as reference samples. Experimental spectra are measured in TEY and shows good agreement with the previous measurements [16, 79]. These are well understood in terms of the calculated atomic transitions $2p^63d^n \rightarrow 2p^53d^{n+1}$ (n = 5 for Mn^{2+} and n = 4 for Mn^{3+}) in an octahedral crystal field. Details of these calculations are provided in the second paragraph of section 5.1 in this chapter. The experimental spectra are dominated by the strong multiplet effects due to Coulomb and exchange interactions between 2*p* core holes and 3*d* electrons.

Almost all of the spectral structures are reproduced in the calculation and the mismatch is attributed to the degree of covalency in the compound and lower symmetry effects [76].

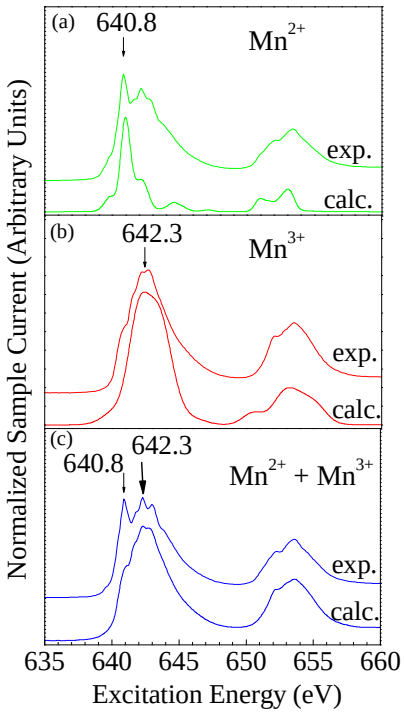

Figure 5.2 Comparison between the experimental Mn 2*p* XAS TEY spectrum and atomic multiplet calculation of (a) Mn^{2+}, (b) Mn^{3+}, and (c) Mn^{2+} + Mn^{3+}. A vertical offset is added to the experimental spectra.

Figure 5.2 shows that the peak at 640.8 eV is typical for Mn^{2+} and the peak around 642.3 eV is typical for Mn^{3+}. Therefore, a substance carrying a mixture of Mn^{2+} and Mn^{3+} is expected to show a double-peak L_3-feature as we see in Figure 5.2(c), which displays both peaks. Now combining the insight from Figure 5.1 and Figure 5.2, it can be concluded that $La_{1-x}Ca_xMnO_3$ sample surfaces contain a mixture of Mn^{2+} and Mn^{3+}. The spectrum for x = 0.20 is very similar to that of Mn^{2+}. Also, comparison of the spectra of x = 0.21, 0.23, and 0.25 to the spectrum of Mn^{2+} + Mn^{3+} yields similarity; showing an initial sharp peak at 640.8 eV characteristic of Mn^{2+} followed by a second peak at 642.3 eV, which is indicative of Mn^{3+}. Decrease of peak-intensity at 640.8 eV with increasing Ca-concentration indicates reduction of Mn^{2+} and on the other hand, increase of peak-intensity at 642.3 eV indicates increase of

Mn^{3+}. This can be explained by saying that increase of Ca^{2+} by replacing La^{3+} obliges Mn to give out more electrons to oxygen, and thus increasing Ca-concentration causes Mn-valency to increase.

Figure 5.3 shows a comparison between the experimental Mn 2*p* TEY XAS and the calculated fit for x = 0.20 and x = 0.21 samples. Fits are calculated using the superposition of the experimental reference spectra of MnO (Mn^{2+}) and $LaMnO_3$ (Mn^{3+}). In this case, $LaMnO_3$ is used as a reference material for Mn^{3+} instead of Mn_2O_3 as $LaMnO_3$ is compositionally close to $La_{1-x}Ca_xMnO_3$ and expected to give a better fit as XAS is strongly affected by the local structure about the absorbing atom. Fit and experimental spectra agree well; all of the experimental features are reproduced in the fit. The fit gives quantitative information regarding the ratio of Mn^{2+} and Mn^{3+} in the samples. It is found that the x = 0.20 sample contains 61% (± 8%) of Mn^{2+} and 39% (± 8%) of Mn^{3+} whereas x = 0.21 sample contains 26% (± 4%) of Mn^{2+} and 74% (± 4%) of Mn^{3+}.

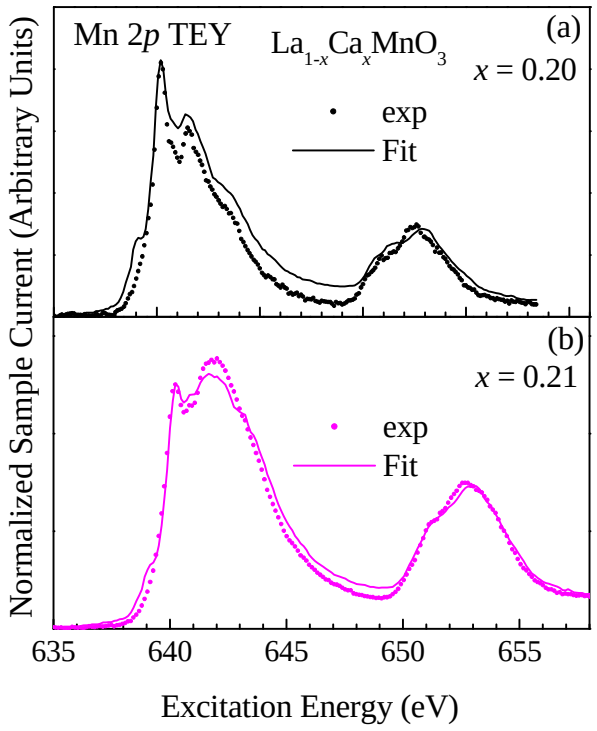

Figure 5.3 Comparison between the experimental Mn 2*p* XAS TEY data (dotted) and constructed fit (solid line) for (a) x = 0.20 and (b) x = 0.21 sample.

In Figure 5.3 one can see that only 1% increase in the Ca-concentration reduces Mn^{2+} approximately two times. The observation described above supports the findings of ref. 74, where it is reported that despite a very small compositional difference between these two samples, they show significantly different zero-field AC susceptibility. This abrupt change is possibly related to the Ferromagnetic Metal (FM) – Ferromagnetic Insulator (FI) transition above the doping level $x = 0.20$ for this system.

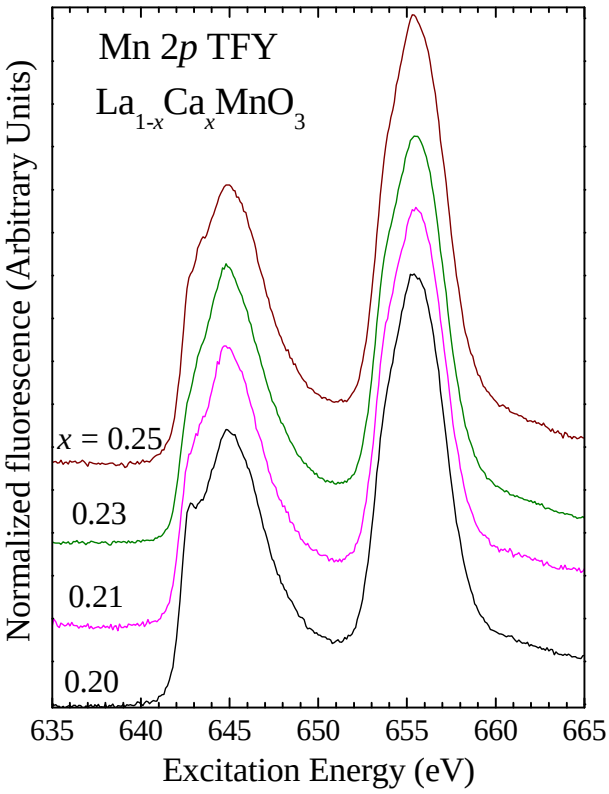

Figure 5.4 Mn 2*p* XAS TFY spectra of $La_{1-x}Ca_xMnO_3$ single crystals. A vertical offset is added to the spectra for clarity.

Figure 5.4 shows Mn 2*p* TFY XAS spectra of $La_{1-x}Ca_xMnO_3$ samples. TFY measurements have depth sensitivity on the order of 150 nm at this energy [80] which is approximately 30 times larger than that of TEY measurements. Comparison between $La_{1-x}Ca_xMnO_3$ TEY (Figure 5.1) and $La_{1-x}Ca_xMnO_3$ TFY (Figure 5.4) indicates that the composition of Mn-valence in $La_{1-x}Ca_xMnO_3$ is depth dependent. The peak at 640.8 eV is particularly suppressed in the TFY measurement, suggesting that Mn^{2+} species are confined only to the surface of

$La_{1-x}Ca_xMnO_3$ (x = 0.20, 0.21, 0.23, and 0.25) and not extended throughout the volume. A minor peak of Mn^{2+} in TFY data for x = 0.20 sample can be attributed to the minor contribution of photons emitted from the surface in this TFY measurement. In addition, nonresonant Mn $L_{2,3}$ XES ($3d4s \rightarrow 2p$ transition) of $La_{1-x}Ca_xMnO_3$ samples is also measured and it is observed that data do not show any concentration dependence. XES is another bulk sensitive technique and the observation suggests that partial densities of the occupied states for the bulk part of the samples are identical. Thus, TFY and XES measurements suggest that electronic structures for the bulk part of the samples are alike.

Figure 5.5 shows Mn $2p$ TEY spectra of $La_{1-x}Ca_xMnO_3$ single crystals post-annealed at 1000 °C for 2 hours in air. The Mn^{2+} content is expected to change by oxygenation procedure [11]. Figure 5.5(a) shows that spectra for various Ca-concentrations are similar and do not show Mn^{2+} related surface induced low energy fine structures. Figure 5.5(b) and Figure 5.5(c) show comparison between the data of as-grown and post-annealed samples for x = 0.20 and 0.21. One can see that annealing strongly suppresses surface Mn^{2+}. A convincing explanation of Mn^{2+} reduction due to annealing is that post-annealing in air changes Mn $3d$-occupancy through oxidization. Oxygen is strongly electronegative and it takes electrons from manganese, consequently converting Mn^{2+} into Mn^{3+}. Also, high-temperature annealing is expected to leave a relaxed sample surface relatively free from surface impurity and symmetry disorder. In ref. 13 authors reported that high temperature annealing at 1000 °C in air changes the observed surface magnetic and transport properties of $La_{2/3}Ca_{1/3}MnO_3$ thin films towards the bulk values. This analysis also supports that observation and shows that post-annealed spectral features are equivalent to Mn^{3+} and also similar to the Mn $2p$ TFY representing the bulk of the samples.

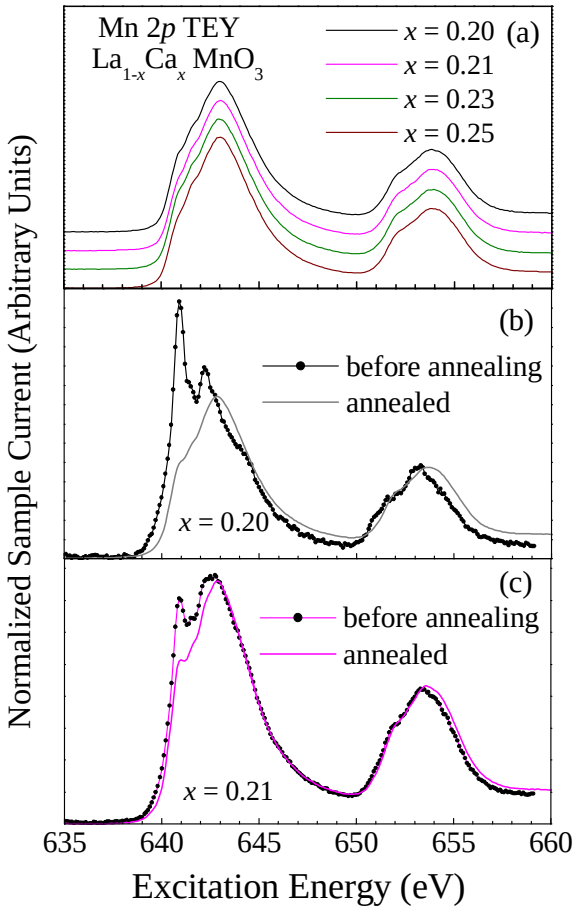

Figure 5.5 (a) Mn 2*p* XAS TEY spectra of the post-annealed $La_{1-x}Ca_xMnO_3$ samples. A vertical offset is added for clarity. (b) Comparison between as-grown and post-annealed spectra of $x = 0.20$. (c) Comparison between as-grown and post-annealed spectra of $x = 0.21$.

O 1*s* XAS. Figure 5.6 shows O 1*s* XAS spectra of as-grown $La_{1-x}Ca_xMnO_3$ measured in TEY (top) and TFY (bottom) detection mode. These spectra originate from the transition of the O 1*s* electron to the unoccupied O 2*p* states and O 2*p* hybridized with Mn 3*d*-states. The spectra are normalized to the peak height at approximately 536.2 eV (the maximum of peak *B*). The spectra show three main features *a*, *b*, and *c* at 529.6, 534.8 - 536.4, and 541 - 544.3 eV, respectively. According to ref. 13, the broad peak *c* is attributed to the bands of higher energy metallic states, e.g., Mn 4*sp* and La 6*sp* bands, while peak *b* is attributed to the bands of primarily La 5*d*-states. The feature associated with the Mn valency is peak *a*, which stems

from the hybridized O 2*p*–Mn 3*d* states. The intensity of peak *a* can be used as a measure of Mn 3*d*–state occupancy. In Figure 5.6(a), we observe an increase of the intensity of peak *a* with increasing Ca-concentration. The intensity of peak *a* for x = 0.21 and 0.23 is similar, which is not surprising because Mn 2*p* TEY spectra of x = 0.21 and 0.23 also show very minor difference. Increase of the peak intensity indicates lower Mn 3*d*–state occupancy, i.e., higher Mn valency. The lower relative intensity of peak *a* for x = 0.20 and 0.21 with respect to x = 0.25 suggests a lower Mn valence for them, which agrees with our previous finding and supports the presence of Mn^{2+} at the sample surface. Figure 5.6(b) shows bulk sensitive TFY spectra of the sample set, which do not show any concentration dependence of the intensity of peak *a*, which agrees with our previous observation that Mn^{2+} is restricted to the sample surface.

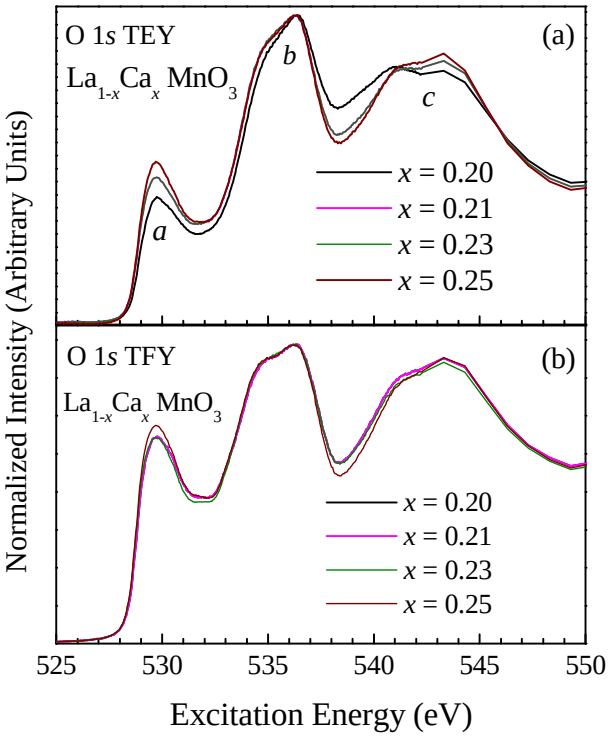

Figure 5.6 O 1*s* XAS (a) TEY and (b) TFY spectra of as-grown $La_{1-x}Ca_xMnO_3$ (x = 0.20, 0.21, 0.23, and 0.25).

The origin of Mn^{2+} is interpreted by suggesting a charge disproportionation model based on the instability of Mn^{3+} for the Mn^{2+} formation via $2Mn^{3+} \rightarrow Mn^{2+} + Mn^{4+}$ by Hundley *et al.* [14] and de Jong *et al.* [11]. However, such mechanism can not explain the formation of Mn^{2+} species solely at the surface and also present analysis does not show Mn^{4+} as expected in the model. A convincing explanation is the possible presence of oxygen vacancy created due to the termination of the periodicity at the surface.

5.1.2 Conclusion

To conclude, a high resolution Mn 2*p* and O 1*s* X-ray absorption spectra of $La_{1-x}Ca_xMnO_3$ (x = 0.20, 0.21, 0.23, and 0.25) single crystals are presented showing the presence of Mn^{2+} at the surface. Comparison of the bulk sensitive TFY spectra with the surface sensitive TEY spectra reveals that Mn^{2+} ions are localized only at the surface and do not extend throughout the bulk of the samples. It is observed that the concentration of Mn^{2+} on the surface is a function of Ca-concentration and can be controlled by changing the amount of the Ca-dopant in the sample. An interesting observation is that only 1% increase of the Ca concentration (from x = 0.20 to x = 0.21) gives the reduction of Mn^{2+} species more than two times, which is explained by FM-FI phase transition. Annealing at 1000 °C strongly suppresses the formation of Mn^{2+}.

5.2 Electronic structure of fundamental Mn oxides

An electronic structure study of four fundamental Mn oxides (MnO, Mn_2O_3, Mn_3O_4, and MnO_2) using soft X-ray spectroscopy is presented to investigate the relative sensitivity of Mn *L*-edge and O *K*-edge to bonding and Mn valency. Low-lying excited states such as *dd*-excitations and charge transfer excitations are probed by RIXS. Four Mn oxides purchased from Sigma-Aldrich with 99.99% purity are measured in this study. Mn *L*-edge and O *K*-edge XAS spectra are measured in the undulator based SGM beamline at the CLS with the energy step size of 0.1 eV. Both surface sensitive and bulk sensitive XAS data are measured using TEY and TFY detection mode, respectively. Resonant X-ray emission data are measured at the beamline 8.0.1 at the ALS. The resolution of the incident beam is controlled by changing the monochromator slits. For XAS measurement the resolving power was set to $E/\Delta E \sim 4000$, however, for resonant XES measurement the resolving power was reduced to $E/\Delta E \sim 700$ as

slits were opened to increase the flux. For emission measurements, the incident flux must be increased to create sufficient core holes so that the two competing processes, radiative decay and Auger decay can result in a good signal to noise ratio. The spectrometer resolution was set to E/ΔE ~ 500. All Mn $L_{2,3}$-edge spectra at the ALS are measured with high energy grating (HEG) of the monochromator and 3rd harmonic of the undulator, whereas O 1s spectra are measured using medium energy monochromator grating (MEG) and 3rd harmonic of the undulator. Every spectrum is recorded at room temperature and is normalized to the number of photons falling on the sample monitored by a highly transparent gold mesh. All measured spectra are calibrated before analysis so that spectra measured at different times can be compared in an absolute energy scale. For calibration purpose, a reference sample with a known spectrum is always measured to calibrate the energy scale of the measured spectra. To calibrate the data, the spectrum of the reference sample is shifted to match the energy scale of the published one and accordingly, the whole set of measurements are shifted by the same amount.

5.2.1 XAS Data Analysis

Figure 5.7 and Figure 5.8 show O 1*s* XAS (1*s* → 2*p* transition) data of four Mn oxides measured in TEY and TFY mode, respectively. Experimental spectra show good agreement with the previous works [16]. Insets are shown to magnify the shift in the absorption edge. BGO is considered as a reference material for calibration purpose as energy positions for the BGO spectrum is well known. Prior to all measurements, O 1*s* XAS of BGO is measured and the data are used to calibrate the series of Mn oxides spectra. One can see that the TFY data (Figure 5.8) for MnO is different from TEY (Figure 5.7). This can be well explained by the oxidization of MnO surface due to air exposure that turns MnO surface close to Mn_3O_4. It is the TEY that detects this surface oxidization as it is a surface sensitive measurement. The spectral features in the O 1*s* XAS of Mn oxides arise from the covalent mixing of the O 2*p* states with Mn 3*d*- and/or 4*sp*-states. According to ref. 81, the spectra can be divided into two main regions. The first region is the double-peaked feature near the absorption threshold that arises from the mixing of O 2*p* with predominantly Mn 3*d*-character [81]. A gradual decrease observed in the intensity of this region from Mn^{4+} (d^3- oxide) to Mn^{2+} (d^5- oxide) can be attributed to the decrease in the number of unoccupied Mn 3*d* states available for mixing with

O 2*p* states. The double peak feature is identified to originate from the ligand field splitting of *d*-states into t_{2g}- and e_g-states [81]. The splitting (Δ) between t_{2g}- and e_g-states is calculated from the O 1*s* XAS TFY and compared (Table 5.1) with the crystal field value obtained from the atomic multiplet calculation of Mn 2*p* XAS of Mn oxides presented in Figure 5.10. Note that Table 5.1 does not contain the data of Mn_3O_4 because the calculated spectrum is obtained by adding the calculated spectra of MnO and Mn_2O_3. Considering the precision in the determination of Δ, a good agreement of the crystal field splitting value is found between experiment and calculation. The second region in the O1*s* XAS of Mn oxides is the broad peak (typically, 5 – 10 eV above the absorption edge) that arises from the hybridization of O 2*p*-states with the Mn 4*s*- and/or 4*p*-states [81].

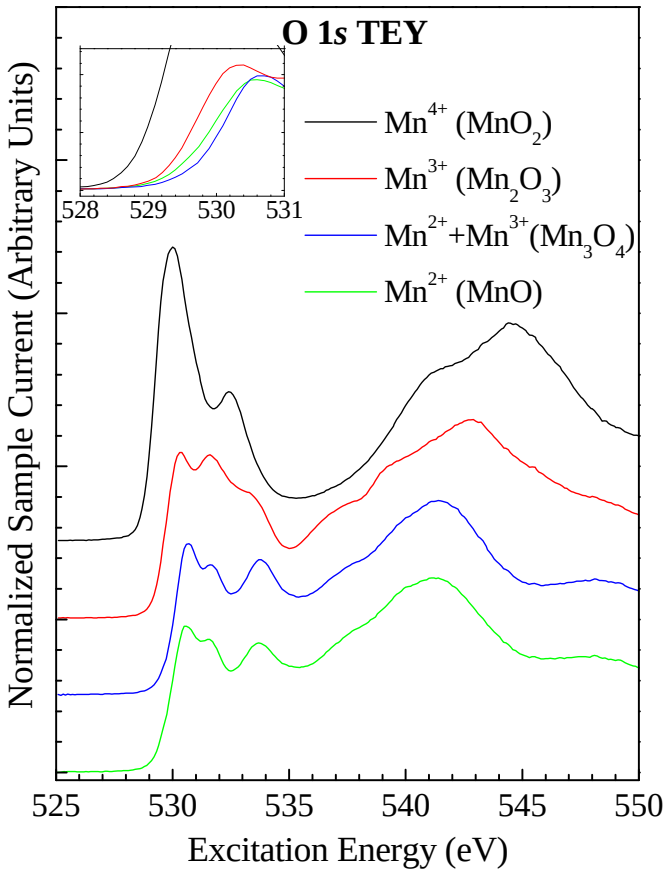

Figure 5.7 O 1*s* XAS TEY data of four Mn oxides. Inset shows magnified energy shift in the absorption edge.

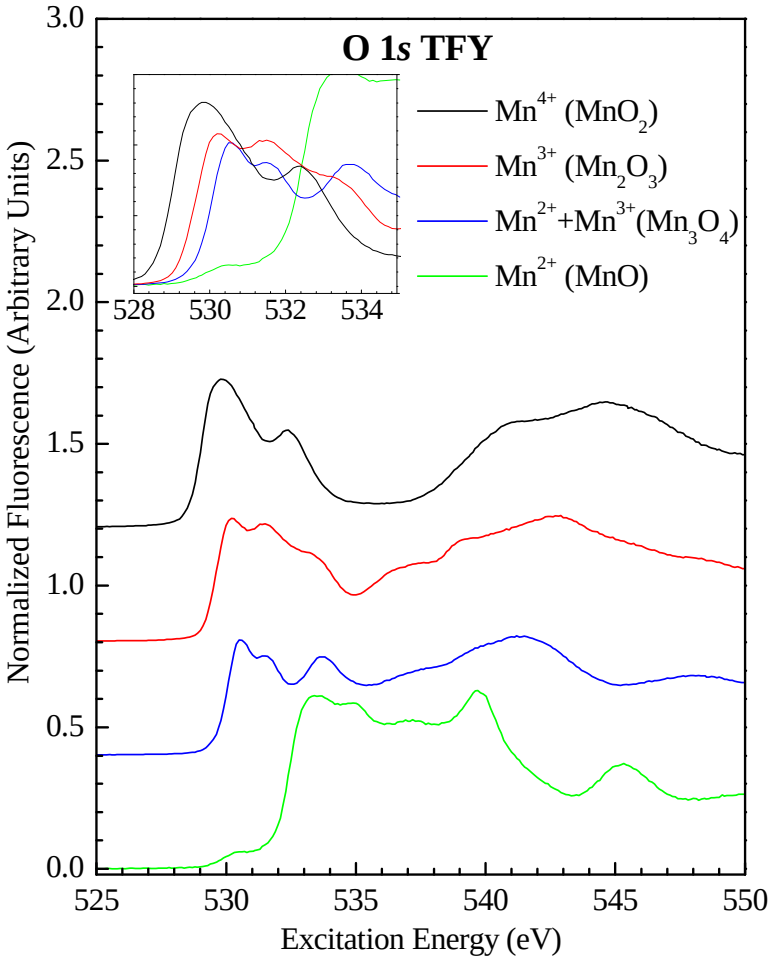

Figure 5.8 O 1*s* XAS TFY data of four Mn oxides. Inset shows magnified energy shift in the absorption edge.

Table 5.1 Comparison of crystal field splitting values.

Compound	Δ from O 1*s* XAS (eV)	Δ obtained from the calculation of Figure 5.8 (eV)
MnO	1.0	0.9
Mn_2O_3	1.4	1.1
MnO_2	2.7	2.7

The high energy spread of the broad feature of O 1*s* XAS data is related with the degree of covalency in the material [81]. One can see that this is clearly visible in both TEY (Figure 5.7) and TFY (Figure 5.8) data. Covalency in Mn-O bond increases with increasing Mn-valence [16], and in accordance with this, the high energy spread of the broad feature increases sequentially as follows: MnO < Mn_3O_4 < Mn_2O_3 < MnO_2. A most striking observation in O 1*s* XAS (both TEY and TFY) of Mn oxides is the gradual shift of the O *K*-absorption edge toward the lower energy by several eV with increasing Mn-valency. The absorption edge for Mn_3O_4 (mixture of Mn^{2+} and Mn^{3+}) is expected to be positioned in between the individual absorption edge of Mn^{2+} and Mn^{3+}. The TFY data in Figure 5.8 clearly shows this but it is not well observed in the TEY data in Figure 5.7. This can be explained by the surface oxidization of Mn_3O_4 due to air exposure. This shift of the absorption edge can be used as a quick tool for chemical valence investigation of Mn in complex systems.

Figure 5.9 shows Mn 2*p* XAS TEY (2*p* → *d*-symmetry transitions) spectra of Mn oxides. In this case MnO is measured as a calibration standard. Experimental spectra agree with previously published data [16, 82]. The spin-orbit splitting of the 2*p* core level gives two edges in the spectra, namely $2p_{3/2}$ (L_3 -edge) and $2p_{1/2}$ (L_2 -edge) separated by ~11 eV. The other spectral features arise from the 2*p*-3*d* and 3*d*-3*d* Coulomb and exchange interactions, as well as crystal field effects. One can see that the spectral shape varies with Mn-valence states. These distinct spectral shapes are representative of the oxidation states as arising from the *d*-state occupancy. It is found that integrated spectral intensity gradually increases from Mn^{2+} to Mn^{4+} (6.57 for Mn^{2+}, 6.79 for Mn^{2+}+ Mn^{3+}, 7.45 for Mn^{3+}, and 8.56 for Mn^{4+}; intensities are in arbitrary units), which is in agreement with the fact that unoccupied *d*-states are increasing from Mn^{2+} to Mn^{4+} (d^5 to d^3). The Mn 2*p* XAS also shows gradual shift in Mn 2*p*-absorption edge for the oxides but shows an opposite trend to what is seen in the O 1*s* XAS. One can see that the edge is shifted toward higher energy as the Mn-valence increases from Mn^{2+} to Mn^{4+}. The inset shows this clearly. A similar chemical shift is observed in Fe 2*p* XAS of divalent and trivalent Fe-ions [83, 84], Cr 2*p* XAS of divalent, trivalent, and hexavalent Cr-ions [85], and the Ni 2*p* XAS [86] data.

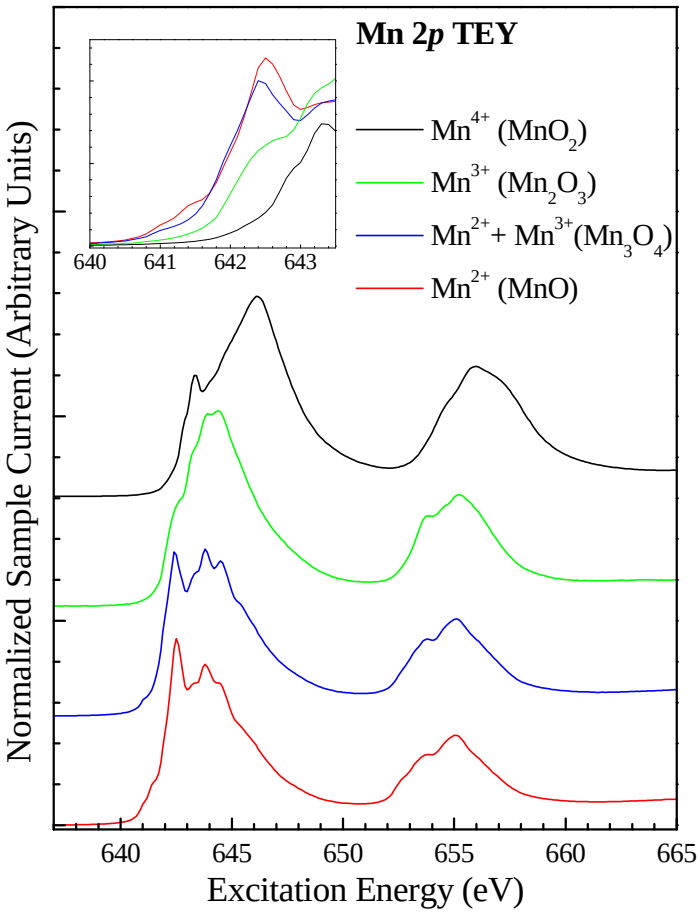

Figure 5.9 Mn 2*p* XAS TEY data of four Mn oxides.

Figure 5.10 shows the comparison of experimental Mn 2*p* XAS of Mn-oxides spectra with atomic multiplet calculations. The atomic multiplet calculations are performed using the crystal field atomic multiplet programs originally written by B. T. Thole [53, 56] and later modified by Jason Sadowski, Mark Hlady, and Adrian Hunt at the University of Saskatchewan (Appendix A). Calculations are carried out by considering the transitions $2p^6 3d^n \rightarrow 2p^5 3d^{n+1}$ (n = 5 for Mn^{2+}, n = 4 for Mn^{3+}, and n = 3 for Mn^{4+}). The Coulomb and exchange parameters, i.e., the so-called Slater integrals are reduced to 80% of the HF values to include the intra-atomic configuration interaction. Mn oxides can be approximated by octahedral symmetry [16] and octahedral crystal field of 0.9 eV, 1.1 eV, and 2.7 eV are used to calculate the best fit for the experimental Mn 2*p* XAS of MnO, Mn_2O_3, and MnO_2,

respectively. These values of crystal field parameters are in close agreement with refs. 58, 75, and 87 and also with the result obtained from the O 1*s* XAS spectra (Table 5.1). A Gaussian broadening of 1.0 eV, 1.5 eV, and 1.2 eV is applied to simulate MnO, Mn_2O_3, and MnO_2, respectively. An equal broadening is applied to every line of the spectrum. Broadening factors and crystal-field parameters are chosen so that the calculated spectra give the best fit to the experiment. To compare with the experiment, calculated spectra are shifted by few eV. The calculated spectrum of Mn_3O_4 (Mn^{2+} + Mn^{3+}) is obtained by the weighted superposition of individually calculated MnO (Mn^{2+}) and Mn_2O_3 (Mn^{3+}). Relative weights of 30% (± 5%) of Mn^{2+} and 70% (± 5%) of Mn^{3+} are used in the calculation. This method provides a good way of generating mixed-valence spectra as long as the local symmetry is same [82].

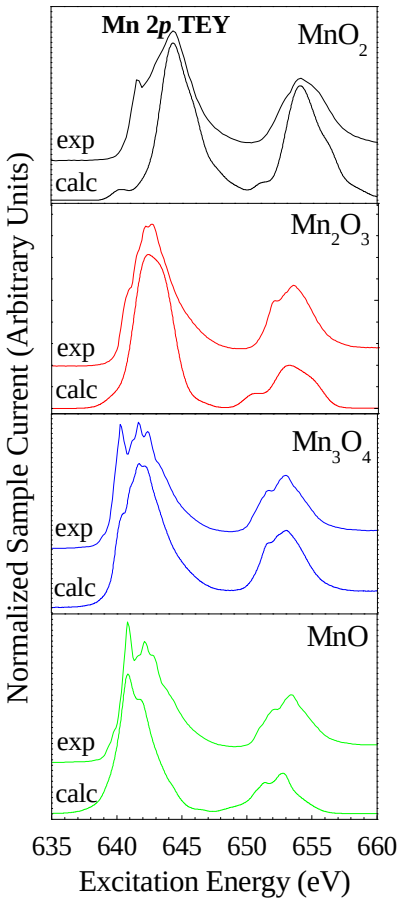

Figure 5.10 Comparison of experimental Mn 2*p* XAS TEY data with atomic multiplet calculations.

One can see in Figure 5.10 that the theoretical simulation reproduces the main features of the experiment reasonably well. The lack of agreement between the calculation and experiment for Mn_2O_3 and MnO_2 can be attributed to the fact that covalency and lower symmetry become more prevalent for these oxides [82, 76]. Ionic compounds or a compound with less covalency are found to show better agreement with atomic calculations [76] because ionic bonds are formed via electron exchange (transfer) resulting in an integer number for the *d*-count that makes the calculation of the atomic transition $2p^6 3d^n \rightarrow 2p^5 3d^{n+1}$ accurate. On the other hand, covalent bonds are formed through electron sharing resulting a non-integer *d*-count, which makes the calculation of atomic transition $2p^6 3d^n \rightarrow 2p^5 3d^{n+1}$ inaccurate. Distorted octahedral symmetry could be considered as another possible reason for the lack of agreement.

5.2.2 RIXS Data Analysis

Mn $L_{\alpha,\beta}$ RIXS is used to probe the intra-atomic *d-d* excitations and the inter-atomic charge transfer excitations. The observed *d-d* excitation features are reproduced by using atomic multiplet calculations and compared with the experiment. Charge transfer excitations are identified in the experimental spectra but not attempted to reproduce in the calculation. In RIXS experiment, a core electron is excited to an unoccupied state and X-ray emission resulting from the decay of the excited state is analyzed. If the emitted energy in the emission process is equal to the excitation energy of the incident photon, i.e., the core-hole created in XAS is being filled by the transition of valence electron (e.g., $2p \rightarrow 3d \rightarrow 2p$ in Mn $L_{\alpha,\beta}$) then the resulting feature in the RIXS spectrum is called recombination peak or elastic peak. On the other hand, if the emitted energy is less than the excitation energy, where transition happens to a low-lying *d*-state then the resulting features are called *d-d* transitions. Consequently, RIXS allows us to probe *d-d* excitations in transition metal oxides. These features are dipole forbidden and therefore produce faint spectra in optical spectroscopy but modern bright sources of X-rays makes it possible to measure these transitions with synchrotron radiation. These dipole forbidden direct transitions are not forbidden in a scattering process. Electron energy loss spectroscopy (EELS) can be used to study *d-d* excitations in transition metal oxides but these measurements are very surface sensitive. RIXS has proven successful to investigate the nature of localization of the 3*d*-electrons for strongly correlated systems in several previous works [45, 88, and 89]. Another important advantage

of RIXS is that the spectral resolution is not affected by the core-hole lifetime and therefore can provide multiplet structure of the ground state configuration [90].

Figures 5.11, 5.12, 5.13, and 5.14 show the comparison of experimental Mn $L_{\alpha,\beta}$ RIXS spectra of MnO, Mn_2O_3, Mn_3O_4, and MnO_2, respectively measured at different excitation energies with their atomic multiplet calculations. The atomic multiplet calculations are carried out using Cowan's programs [54], which do not consider crystal field effects (Appendix B). The Slater integrals are scaled down to 80% of their HF values to account for the intra-atomic configuration interaction effects. A Gaussian broadening of 0.5 eV, 0.7 eV, and 0.3 eV is applied to simulate MnO, Mn_2O_3, and MnO_2 spectra, respectively. Experimental RIXS spectra are displayed on an energy loss scale as it helps identifying some of the final states easily. Mn 2*p* XAS of each Mn oxides are measured prior to RIXS measurement in order to determine the excitation energies to be used in RIXS experiment. In the figures, letters associated with each RIXS spectrum represents the excitation energy taken from the XAS data shown on top of each figure. MnO is used as a calibration standard to calibrate the data set. RIXS shows three features: recombination peak, loss features due to *d*-*d* excitation, and charge-transfer features involving transfer of an electron from O^{2-} ligand to Mn. Figure shows that each spectrum consists of strong multiplet structures and the intensity of all features is dependent on the excitation energy. The peak corresponding to the energy loss of 0 eV represents the elastic peak. One can see that the intensity of the elastic peak decreases with increasing excitation energy. This is interpreted as a consequence of spin ordering of the excited states [89]. It is said that the lowest $2p^5 3d^6$ intermediate states are more likely to decay into the ground state as both of these states are sextets (^6S) and therefore, spin conserves in the transition. Hence, the lowest intermediate states strongly contribute to the elastic peak. But the higher energy states in the intermediate state (which are quartets and doublets) are less likely to decay into the ground state and therefore contribute less to the elastic peak. It can also be explained by saying that weaker absorption at higher excitation causes low emission.

Figure 5.11 shows the Mn $L_{\alpha,\beta}$ RIXS spectra of MnO with atomic multiplet calculations. The corresponding transition is $2p^6 3s^2 3p^6 3d^5 \rightarrow 2p^5 3s^2 3p^6 3d^6 \rightarrow 2p^6 3s^2 3p^6 3d^5$. Spectra are displayed on the energy loss scale by subtracting excitation energy from the emission

energies. Features at zero energy loss are the elastic peaks. At the excitation energy of 638.5 eV (a) and 639.2 eV (b) RIXS results in a single peak at around 3.5 eV of energy loss while the spectra are dominated by the elastic peak. Theoretical analysis using the atomic multiplet calculations show that the inelastic peaks at the energy loss of 3.5 eV are due to the transition to ${}^4G$, ${}^4D$, and ${}^4P$ derived final states. When the excitation energy is tuned to 640.5 eV (c), a shoulder starts to appear at the energy loss of around 5 eV which grows continuously with increasing excitation energy. The calculation shows that this feature at around 5 eV results from the transition to the final states of ${}^4F$, ${}^2H$, ${}^2G$, and ${}^2F$ symmetry. These results presented in Table 5.2 are in good agreement with the previous report of MnO RIXS [15]. One can clearly distinguish the *d-d* excitation features from the charge transfer features by comparing the experimental RIXS with the results of atomic multiplet calculation as charge transfer features are not reproduced in the calculation. The broad features around the energy loss of 8 eV and 15 eV are the interatomic charge transfer features.

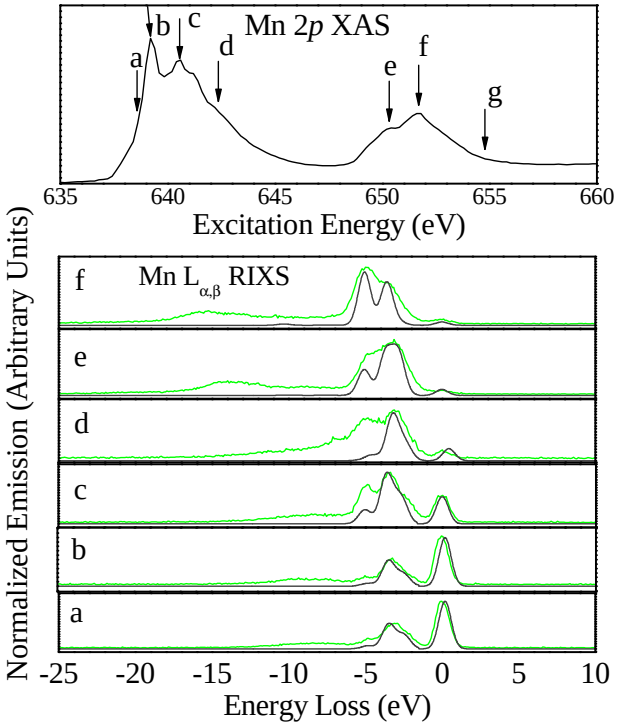

Figure 5.11 Mn $L_{\alpha,\beta}$ RIXS data of MnO (green) plotted as energy loss spectra relative to the elastic peak at 0 eV compared to the atomic multiplet calculation (black). Letters correspond to different excitation energies indicated in the absorption spectrum shown on top.

Table 5.2 Energy loss, initial, intermediate, and final states for the MnO RIXS.

Energy Loss (eV)	Initial state	Intermediate states	Final states
0	^6S	^4P	^6S
3.5			^4G , ^4D , ^4P
5			^2G , ^4F , ^2F , ^2H

Figure 5.12 shows the experimental Mn $L_{\alpha,\beta}$ RIXS spectra of Mn_2O_3 ($2p^6 3s^2 3p^6 3d^4 \rightarrow 2p^5 3s^2 3p^6 3d^5 \rightarrow 2p^6 3s^2 3p^6 3d^4$) along with the results of atomic multiplet calculation. In this case charge transfer features are dominant compared to the case of MnO, which is because Mn_2O_3 is more covalent compared to MnO, and therefore results in more hybridization or charge transfer excitation. The overlap of charge transfer and *d-d* excitation features result in broadened RIXS spectra. However, *d-d* features can be separated from the charge transfer features by looking at the calculations as the charge transfer part is not calculated. The analysis of the atomic multiplet calculation reveals that the energy loss feature at around 2.5 eV is due to ^3F , ^3G , and ^3H derived final states as listed in Table 5.3. This feature is especially pronounced compared to the other multiplet features in the Mn_2O_3 RIXS. Analysis shows that the features corresponding to the energy loss of around 2.5 eV are originating from the transition to the final states of ^3F and ^3H symmetry and shoulder appears at around 5 eV corresponds to ^3F derived final states.

Table 5.3 Energy loss, initial, intermediate, and final states for the Mn_2O_3 RIXS.

Energy Loss (eV)	Initial state	Intermediate states	Final states
0	^5D	^5F , ^5P	^5D
2.5			^3F , ^3H
5			^3F

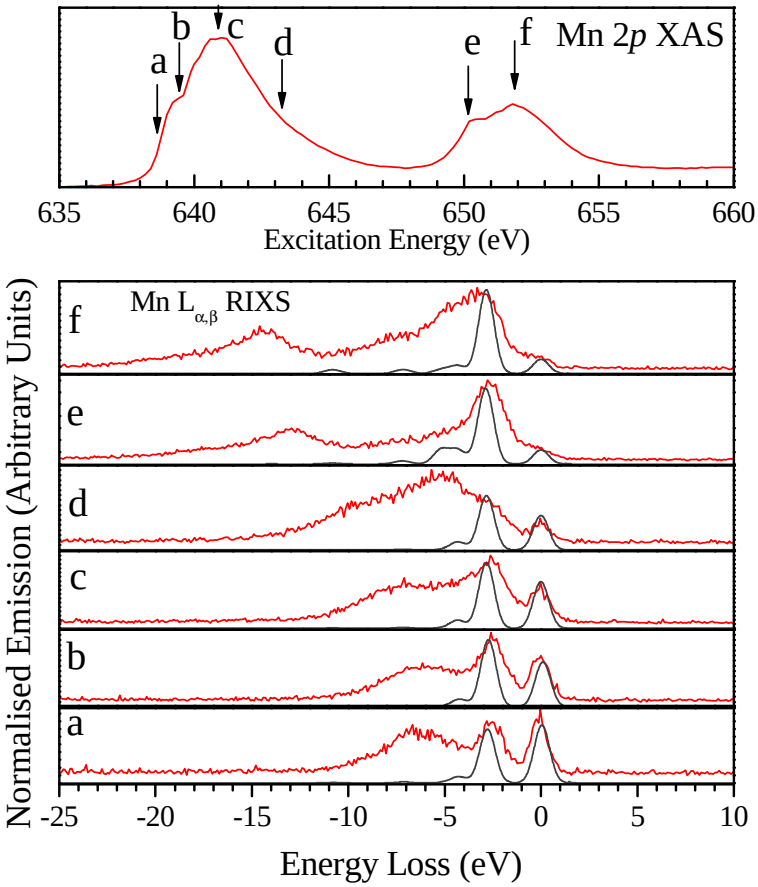

Figure 5.12 Mn $L_{\alpha,\beta}$ RIXS data of Mn_2O_3 (red) plotted as energy loss spectra relative to the elastic peak at 0 eV compared to the atomic multiplet calculation (black). Letters correspond to different excitation energies indicated in the absorption spectrum shown on top.

Figure 5.13 shows Mn $L_{\alpha,\beta}$ RIXS spectra of Mn_3O_4 along with atomic multiplet calculations displayed in energy loss scale. Mn_3O_4 is a mixed Mn^{2+} + Mn^{3+} compound and cannot be calculated directly by the Cowan's program. A weighted linear combination of the individual atomic multiplet calculation result of MnO RIXS and Mn_2O_3 RIXS is used to generate the calculated Mn_3O_4 RIXS spectra. This semi-empirical method is found to be successful as one can see that the experimental RIXS features are reproduced in the calculation.

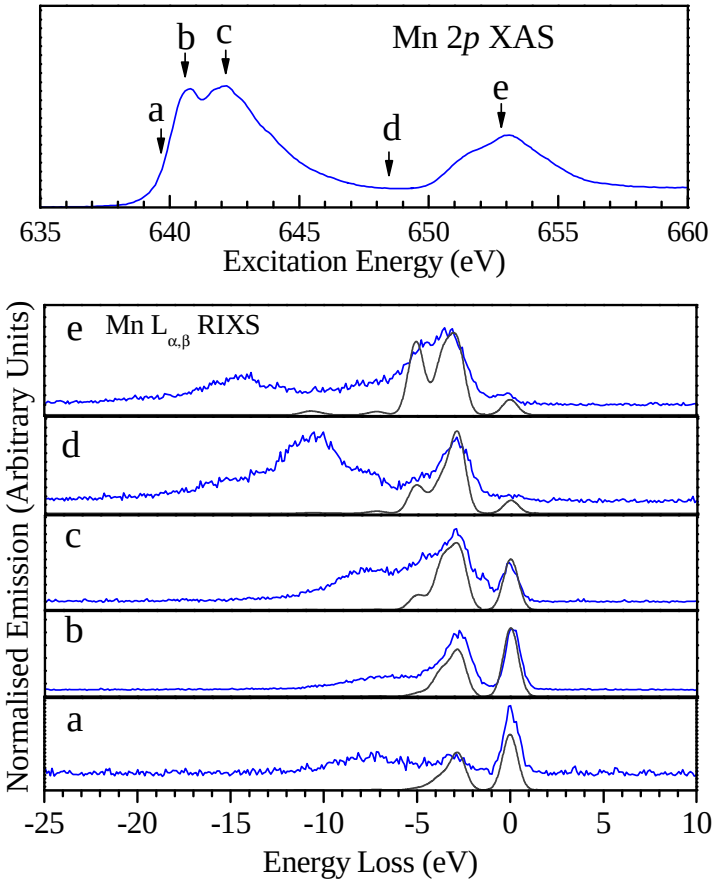

Figure 5.13 Mn $L_{\alpha,\beta}$ RIXS data of Mn_3O_4 (blue) plotted as energy loss spectra relative to the elastic peak at 0 eV compared to the atomic multiplet calculation (black). Letters correspond to different excitation energies indicated in the absorption spectrum shown on top.

Figure 5.14 shows the Mn $L_{\alpha,\beta}$ RIXS spectra of MnO_2 ($2p^63s^23p^63d^3 \rightarrow 2p^53s^23p^63d^4 \rightarrow 2p^63s^23p^63d^3$) along with the atomic multiplet calculations. It is clear that charge transfer excitations ($3d^4\underline{L}$ where $\underline{L}$ represents a hole in the O 2*p* band) are now more prevalent than the previous two cases (MnO and Mn_2O_3). According to the ref. 16, MnO_2 is more covalent than Mn_2O_3 and this is why the charge transfer effects are expected to be more pronounced. Experimental spectra show broad features, which are due to the overlap of *d-d* features and charge-transfer features as well as due to the limitation of spectral resolution. Atomic multiplet calculation is used to separate the charge-transfer satellites and thus to find out the contribution of *d-d* excitations in the spectra. The calculated spectra look reasonable. Results

of the atomic multiplet calculation are listed in Table 5.4. It is found that the energy loss features at 2.5 eV are corresponding to the transitions to ^2G , and ^1I derived final states. Other features at approximately 5 eV are due to ^2G final states.

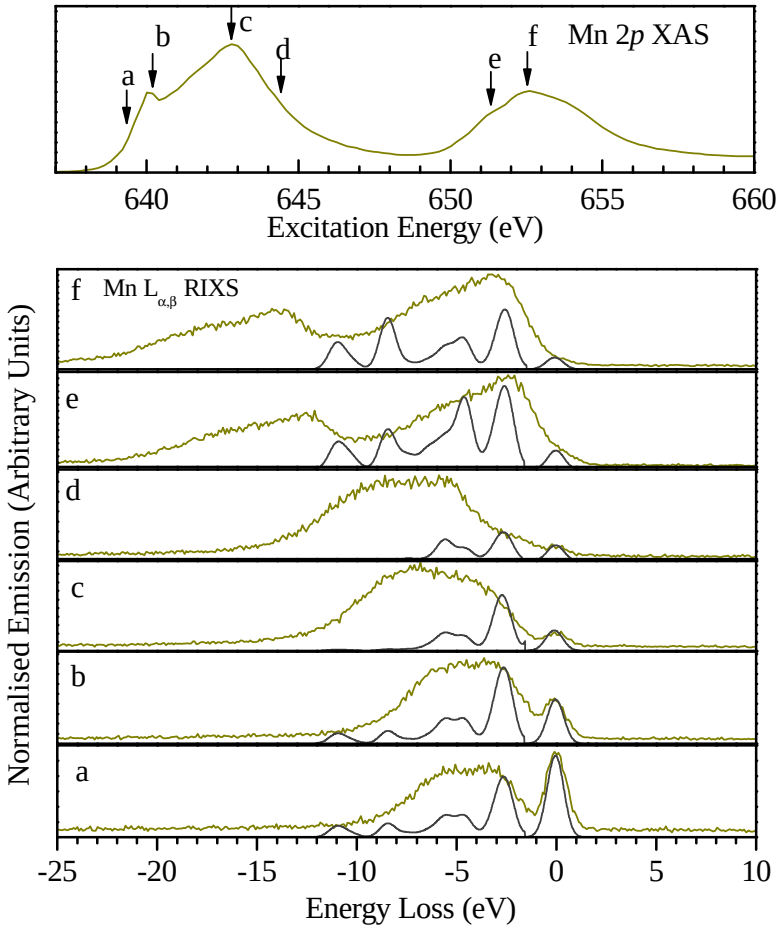

Figure 5.14 Mn $L_{\alpha,\beta}$ RIXS data of MnO_2 (dark yellow) plotted as energy loss spectra relative to the elastic peak at 0 eV compared to the atomic multiplet calculation (black). Letters correspond to different excitation energies indicated in the absorption spectrum shown on top.

Table 5.4 Energy loss, initial, intermediate, and final states for the MnO_2 RIXS.

Energy Loss (eV)	Initial state	Intermediate states	Final states
0	^4F	$^2D, ^4D, ^4G$	^4F
2.5			$^2G, ^1I$
5			^2G

5.2.3 Conclusion

In summary, Mn 2*p* and O 1*s* XAS and Mn $L_{\alpha,\beta}$ RIXS spectra of four Mn oxides (MnO, Mn_2O_3, Mn_3O_4, and MnO_2) are measured and presented in this study. X-ray absorption spectra measured at Mn 2*p*- and O 1*s*-edge are found to be sensitive to the Mn-valence state in Mn-compounds and can be used to determine the Mn-valence in unknowns. Mn $L_{\alpha,\beta}$ RIXS spectroscopy is demonstrated as a powerful tool in describing the low energy excitations, e.g., *d-d* excitations and charge-transfer excited states in transition metal compounds. Atomic calculations are shown to be successful in reproducing *d-d* features of RIXS spectra of Mn oxides.

5.3 Electronic structure of Fe-implanted ZnO

In this study electronic structure of three Fe-implanted ZnO DMS samples are reported using XAS and XES. The goal is to investigate the oxidation state and site symmetry of doped Fe ions in ZnO, and thus to shed light on the controversy of the origin of ferromagnetism. Samples implanted with different ion fluences using both polycrystalline and epitaxial ZnO are chosen for this study to investigate the effect of the ion dose of Fe implantation and the structure of the host ZnO on the sample characteristics. Sample *A* is prepared by a Fe-ion fluence of 1.6×10^{17} cm^{-2} using polycrystalline ZnO, sample *B* is grown with the same fluence but with epitaxial ZnO, and sample *C* is irradiated with a high dose of 8.0×10^{17} cm^{-2} using polycrystalline ZnO. For the measurements, samples were mounted on the sample holder by pressing them on a carbon tape. Fe 2*p*, O 1*s*, and Zn 2*p* XAS spectra are measured at the SGM beamline at the CLS with the energy step size of 0.1 eV. XAS data of Fe oxides such as FeO (Fe^{2+}) and Fe_2O_3 (Fe^{3+}) are also measured to aid the analysis. Fe L_2 -RIXS measurements are performed at the beamline 8.0.1 at the ALS with the 3rd harmonic of the undulator, HEG

of the monochromator, and a monochromator resolving power of E/ΔE ~ 700. All spectra are recorded at RT and normalized to the mesh current. The measured spectra of reference samples are used to calibrate the data set.

5.3.1 XAS Data Analysis

Figure 5.15 shows Fe 2*p* XAS TEY spectra of samples *A*, *B*, and *C* compared to the reference spectra of FeO (Fe^{2+}) and Fe_2O_3 (Fe^{3+}). Spectral intensities are normalized at the intensity of the low-energy peak '*a*'. The Fe 2*p* XAS spectrum originates from the $2p \rightarrow 3d$ symmetry transition. Due to the spin orbit splitting of the 2*p*-state, two main absorption lines appear in the spectra separated by ~12 eV that are associated with the transitions from $2p_{3/2}$ (L_3, ~709 eV) and $2p_{1/2}$ (L_2, ~721 eV) core levels, respectively. One can see that the intensity of the spectral features of Fe-doped ZnO samples changes as a function of Fe ion fluence and also depends on the crystallinity (polycrystalline or epitaxial) of ZnO host semiconductor. XAS spectra of Fe ion implanted samples show a double peak feature at the Fe L_3-edge and three overlapping features at the L_2-edge. Analysis of the reference spectra [FeO (Fe^{2+})] and Fe_2O_3 (Fe^{3+})) shows that the Fe L_3-peak at ~707 eV with a shoulder of the L_2-peak at ~719 eV represents a fingerprint for Fe^{2+}, whereas the Fe L_3-peak at ~708 eV with the L_2-peak features near 720 and 722 eV represents a fingerprint for Fe^{3+}. Comparing with the fingerprints of Fe^{2+} and Fe^{3+}, one can conclude that Fe-doped samples contain a mixture of Fe^{2+} and Fe^{3+} with varying ratio of Fe^{2+}: Fe^{3+}. This observation supports the previously published results [91 - 93].

In Figure 5.15, L_3-peak shows two the main features '*a*' (~ 707 eV) and '*b*' (~ 708.3 eV). Feature '*a*' is dominant in divalent Fe (Fe^{2+}) whereas the feature '*b*' is prominent in the spectrum of trivalent Fe ions (Fe^{3+}). The spectrum *C* with the highest ion influence of 8.0×10^{17} cm^{-2} closely resembles the spectrum of Fe^{2+}. We observe that as the ion fluence decreases from 8.0×10^{17} cm^{-2} (sample *C*) to 1.6×10^{17} cm^{-2} (samples *B* and *A*), the level of Fe^{2+} decreases and conversely, Fe^{3+} increases. This trend suggests that the samples implanted with a low Fe ion dose contain more Fe^{3+}. The origin of Fe^{3+} can be explained by the presence of Zn-vacancy in ZnO matrix [93] that is very likely created due to the bombardment of Fe-ion on ZnO. If there is a Zn-vacancy in the neighborhood of Fe^{2+} (substitutional Zn-site), then

the valence state of Fe^{2+} might be influenced and converted into Fe^{3+} in order to achieve charge neutrality of the sample. It can be argued that in case of samples with the higher Fe dose, Fe^{2+} dominates over the formation of Fe^{3+} because Zn-vacancy related defects are well compensated with lower Fe dose.

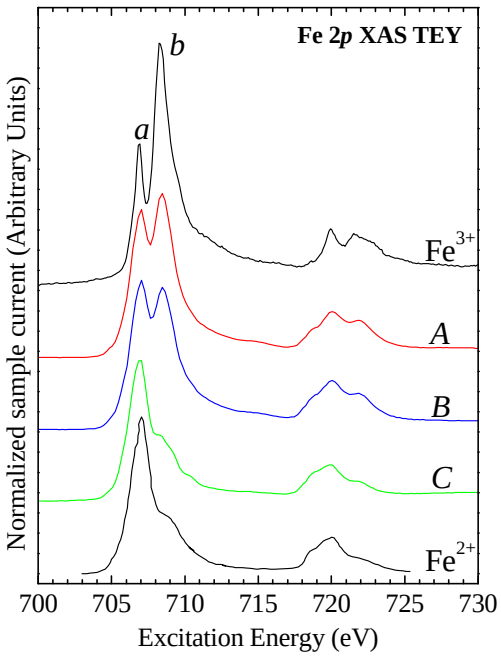

Figure 5.15 Fe 2*p* XAS TEY spectra for samples *A*, *B*, and *C* compared to the reference samples. A vertical offset is added to the spectra.

Figure 5.16 shows the results of the calculation. To gain insight in the coordination geometry of doped Fe ions incorporated into ZnO, atomic multiplet calculations of Fe^{2+} in octahedral and tetrahedral symmetry are performed. Comparing the theoretical results of Figure 5.16 with the experimental Fe 2*p* XAS spectra in Figure 5.15, one can see that the experimental spectral features are consistent with the calculated data of tetrahedral case, suggesting that the coordination environment of Fe dopants is tetrahedral. One can rule out the case of octahedral coordination because the low energy shoulder at ~ 719 eV at the L_2-peak is absent in the theoretical calculation of octahedral case. It is known that Zn ions in ZnO structure are tetrahedrally coordinated with O ligands [93] and therefore the present analysis reveals that Fe

ions incorporated into the ZnO lattice by substituting Zn-sites retains in the original structure of ZnO host semiconductor.

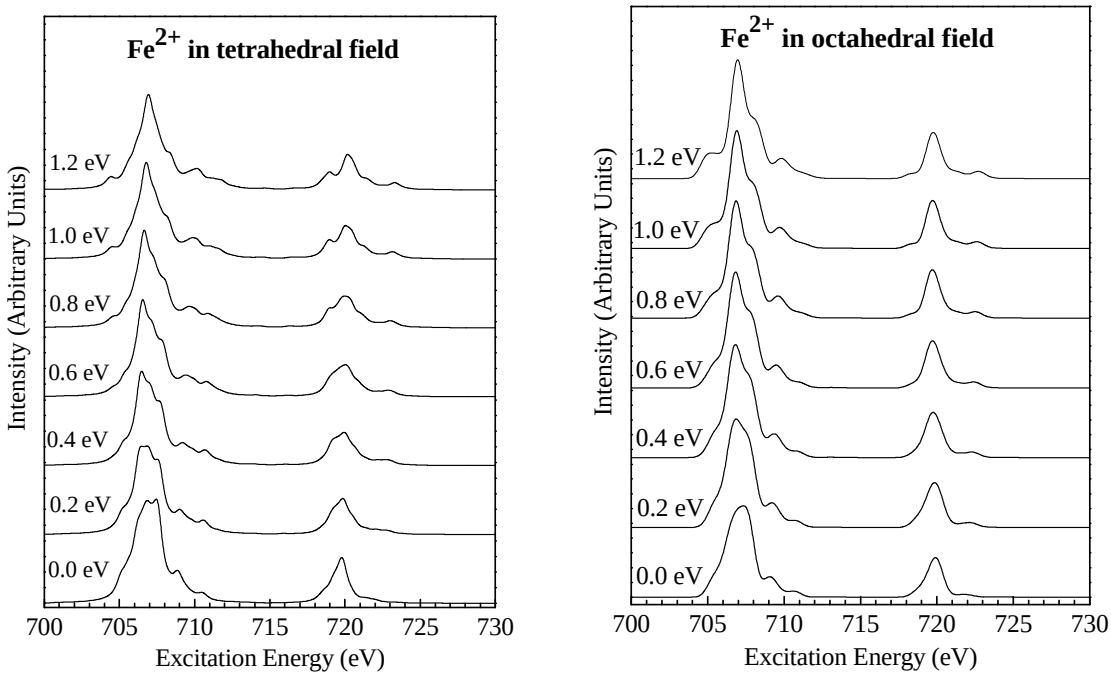

Figure 5.16 Atomic multiplet calculation for Fe^{2+} in different tetrahedral (left) and octahedral (right) field. Vertical offset is added for clarity.

Figure 5.17 shows Zn L_3-edge ($2p_{3/2}$) XAS TEY spectra of Samples *A*, *B*, and *C*. Zn-sites in the ZnO matrix are affected by the Fe ion implantation and therefore it is realistic to study the local electronic structure of Zn. Three weak features at approximately 1012 eV, 1017 eV, and 1022 eV that originate from the transition of Zn $2p_{3/2}$ electrons to Zn 4*s* and antibonding 3*d* states [94]. One can see that there is no noticeable difference among the spectral profiles; overall spectral features are similar for all samples. This observation suggests that the irradiation-induced defects are saturated for the associated ion doses.

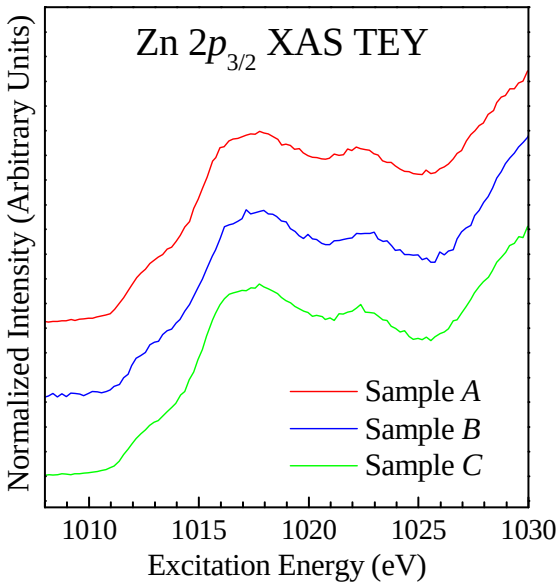

Figure 5.17 Zn $2p_{3/2}$ XAS spectra of Samples *A*, *B*, and *C*.

Figure 5.18 shows the O 1*s* XAS TFY (1*s* → 2*p* transition) spectra of Fe-implanted samples. Fe 2*p* XAS spectra tells us that the Fe dopant ions are incorporated into the Zn-site with surrounding oxygen atoms, therefore, measurement of O 1*s* XAS spectra is useful as it probes the partial density of O 2*p* unoccupied states in relation to the hybridization between O 2*p* orbital and localized Zn 3*d*4*s*/Fe 3*d* orbitals. As described in refs. 95 and 96, the spectral features of O 1*s* XAS spectra for TM-doped ZnO can be described as follows: i) low energy features f_1, f_2, and f_3 below 537 eV are associated mainly with the hybridization between O 2*p* and Zn 3*d*4*s*/Fe 3*d* states, ii) feature f_4 at ~537.5 eV arises from the transition of 1*s* electrons to non-dispersive O $2p_z$ and O $2p_{x+y}$ states, iii) features f_5 and f_6 between 539 eV to 545 eV are due to the hybridization between O 2*p* and Zn 4*p*/Fe 4*sp* states, and iv) features above 550 eV are attributed to the O 2*p* states hybridized with Zn/Fe higher orbitals. In addition, according to ref. 95, the fine structures f_1 and f_2 are originated from the hybridization of O 2*p*-states with the unoccupied t_2-states of Fe 3*d* orbital (crystal-field splitting states of Fe 3*d* orbital is *e* and t_2) and the presence of interstitial occupancy of TM dopants enhances these features, while, based on their first principle calculation, the reduction of feature f_3 is attributed to the

formation of oxygen vacancies (O_v). From Figure 5.18, it is evident that the spectral weight in the low-energy region increases with increasing Fe-concentration except for sample *B*, which is based on an epitaxial ZnO host. For samples *A* and *C*, the observed increase of spectral weight below the feature f_4 suggests a strong hybridization between the O 2*p* and Fe 3*d* orbitals that increases with increasing Fe-doping. On the other hand, sample *B* clearly shows a reduction in feature f_3, which indicates that O_v-defects are induced by Fe-doping in this sample. Intensity of features f_5 and f_6 are significantly enhanced and broadened for the sample *B*, suggesting that hybridization with higher Fe orbital increases for epitaxial ZnO.

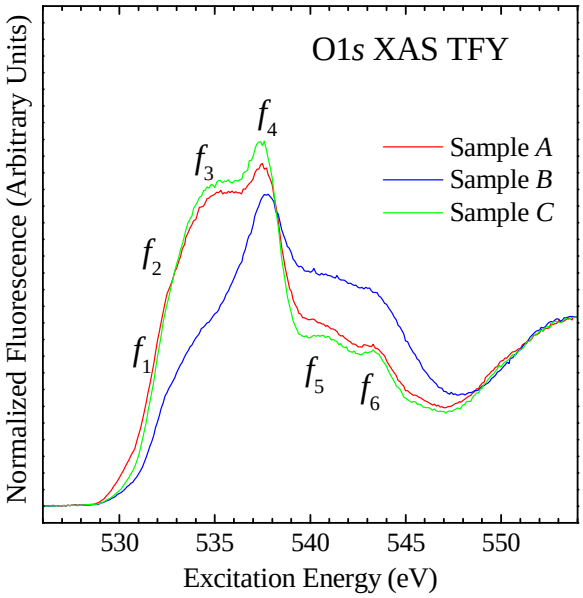

Figure 5.18 O 1s XAS TFY spectra of Samples *A*, *B*, and *C*.

5.3.2 RIXS Data Analysis

In XES, incident radiation excites core electrons to unoccupied conduction states (RIXS) or continuum (nonresonant XES) and subsequently, a valence band electron recombines with the core hole resulting in X-ray emission. Fe $L_{2,3}$ X-ray emission occurs when a transition takes place from 3*d* and 4*s* valence states to the $2p_{3/2}$ (L_3-emission line) and $2p_{1/2}$ (L_2-emission line) core holes, respectively. When the excitation energy is above the L_2 absorption threshold, the ratio of the integrated emission intensities I(L_2)/I(L_3) is expected to be 1:2, as predicted by the

one-electron picture satisfying Fermi's golden rule, based on the $2j+1$ degeneracy of the initial $2p_{1/2}$ and $2p_{3/2}$ core levels. But in reality, this ratio deviates from the value of ½ since radiationless decay occurs through Auger and Coster-Kronig (C-K) transitions. Theoretical expression for the I(L_2)/I(L_3) intensity ratio reported in the previous literature [97] considering multiple decay processes is obtained as follows:

$$\frac{I(L_2)}{I(L_3)} = \frac{1 - f_{2,3}}{f_{2,3} + \mu_3 / \mu_2} \tag{5.1}$$

Multiple decay mechanisms that are taken into account in deriving the above expression are known as i) radiative transitions ii) non-radiative Auger transitions; that involves three orbitals where principal quantum numbers for the first and the second orbitals are different and, iii) radiationless C-K transitions; that involves transitions within the same shell. In this expression $f_{2,3}$ represents the probability of C-K transitions, and μ_3 / μ_2 is the ratio of total photo-absorption coefficients at L_3 and L_2 threshold. It is found that for 3*d*-metals, a ratio of $\mu_3 / \mu_2 = 2$ is a good approximation if the excitation energy is far above the resonance [97]. Therefore, the ratio I(L_2)/I(L_3) only depends on the factor $f_{2,3}$, which is determined by the number of available free carriers [98]. Thus the I(L_2)/I(L_3) ratio gives an account for the variation of charge carriers (sometimes referred to as metallicity) in the experimental sample.

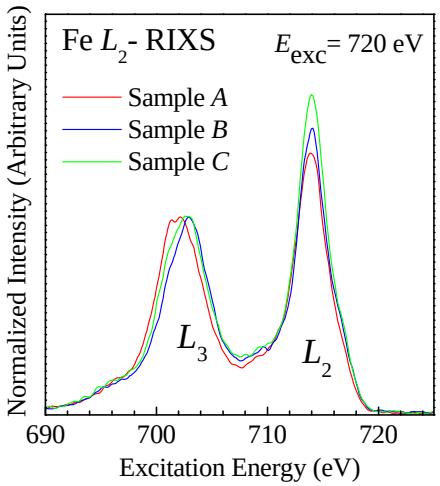

Figure 5.19 Fe L_2 – RIXS spectra of samples *A*, *B*, and *C*.

Figure 5.19 shows Fe L_2-RIXS spectra of samples *A*, *B*, and *C* measured at the excitation energy (E_{exc}) tuned to the L_2-absorption threshold (720 eV). All spectra are normalized to the same L_3-peak height around 703 eV. One can see that the intensity ratio I(L_2)/I(L_3) increases as sample *A* < sample *B* < sample *C*, which implies that the amount of free charge carriers increases as sample *C* < sample *B* < sample *A*. Sample *A* shows the highest number of loosely bound charge carriers around Fe-ions, where sample *A* and sample *B* are made of the same Fe-ion fluence. We know that sample *A* is prepared with polycrystalline ZnO, whereas sample *B* is made of epitaxial ZnO. Therefore, it is reasonable to consider that polycrystalline ZnO provides more intrinsic defects compared to the epitaxial ZnO. Since the defect formation energy for the formation of p-type ZnO is very high [99], n-type ZnO is more likely to occur. Sample *A* (polycrystalline ZnO) is likely to carry more n-type carriers than sample *B* (epitaxial ZnO). This is why, sample *A* suffers from higher C-K transitions resulting in the most reduced L_2-peak intensity in the Fe L_2-RIXS measurement. Sample *C* is made of the highest (8×10^{17} cm^{-2}) Fe implantation dose, and therefore it is likely to form FeO clusters due to very high Fe-ion dose. Note that this ion-dose is really high in accordance with ref. 100, which indicates that Fe fluence of 2×10^{16} cm^{-2} yields an atomic concentration of ~5%. Formation of FeO (insulator) clusters in sample *C* explains the presence of least charge carriers in it.

5.3.3 Conclusion

To conclude, electronic structure of Fe-implanted ZnO samples is studied using soft X-ray absorption spectroscopy and emission spectroscopy. Fe 2*p* XAS measurements reveal that Fe dopant ions exists in mixed Fe^{2+} and Fe^{3+} oxidation states, while Fe^{2+} increases with increasing Fe ion fluence. A combined theoretical and experimental study shows that most of the Fe dopant ions are incorporated into the tetrahedral Zn-sites of ZnO. Fe L_2-RIXS measurement shows indication of FeO cluster formation in sample *C*, whereas sample *A* exhibits more charge carriers around Fe-ions compared to sample *B* and sample *C*.

CHAPTER 6
CONCLUSIONS

A soft X-ray spectroscopic study of the electronic structure of three kinds of transition metal compounds, specifically, Ca-doped $LaMnO_3$, four fundamental Mn oxides (MnO, Mn_2O_3, Mn_3O_4, and MnO_2), and Fe-doped ZnO samples is presented. A combined experimental and theoretical analysis is used to reveal important electronic structure information regarding the studied compounds.

For Ca-doped $LaMnO_3$ (x = 0.20, 0.21, 0.23, and 0.25) single crystals, high resolution manganese 2*p* and oxygen 1*s* XAS spectra are presented for the sample series. The Mn 2*p* XAS spectra are compared with the atomic multiplet calculations in order to determine the valency of Mn-ions. Using surface sensitive measurements, it is found that Mn^{2+} is present in the $La_{1-x}Ca_xMnO_3$ surface, while bulk sensitive measurement confirmed that Mn^{2+} is not extended throughout the samples. The presence of Mn^{2+} on the surface is further confirmed by using oxygen 1*s* XAS measurement. The analysis shows that the Mn^{2+}-concentration is a function of the Ca-concentration in the sample. High temperature annealing at 1000°C is observed to effectively suppress the formation of Mn^{2+}. These results will contribute to the application of these perovskites as magnetoresistive materials since electronic and magnetic properties are governed by the Mn-valence.

Mn oxides are often used as standard reference materials in the research of Mn-related unknown compounds and therefore an established interpretation of manganese 2*p* and oxygen 1*s* XAS is important. The sensitivity of Mn 2*p* XAS and O 1*s* XAS to Mn-valence states is studied for Mn oxides (MnO, Mn_2O_3, Mn_3O_4, and MnO_2). A characteristic shift in the Mn 2*p* absorption edge toward the higher energy is observed with increasing Mn-valence. Also an opposite gradual shift in the O 1*s* absorption edge toward lower energy is observed with increasing Mn-valence. Theoretical calculations using the atomic multiplet code are used successfully to reproduce the observed experimental Mn 2*p* XAS features. Crystal field splitting parameters obtained from the atomic multiplet calculation show good agreement with the values obtained from the experiment. Mn $L_{\alpha,\beta}$ RIXS spectra of MnO, Mn_2O_3, Mn_3O_4, and

MnO_2 are measured at different excitation energies sweeping through the Mn 2*p* XAS spectrum of individual oxides. For the first time, Mn $L_{\alpha,\beta}$ RIXS spectra of Mn_2O_3, Mn_3O_4, and MnO_2 are reported, while the measurement for MnO is previously reported by Butorin *et al.* [15]. Reported results for MnO agreed well with the previously published results [15]. The atomic multiplet calculations are successfully used to reproduce the *d*-*d* excitation features of the RIXS spectra.

Local electronic structures of a series of Fe implanted ZnO samples are investigated using soft X-ray spectroscopy to determine the local environment of doped Fe-ions, which are responsible for the ferromagnetism in these materials. Theoretical and experimental Fe 2*p* XAS is used to determine the oxidation state of doped Fe-ions. Study concludes that Fe-ions in ZnO matrix are present in mixed Fe^{2+} and Fe^{3+} oxidation states, while Fe^{2+} increases with increasing Fe ion fluence. A mechanism for the origin of Fe^{3+} and a possible explanation for the increase of Fe^{2+} with increasing Fe ion fluence are proposed. Atomic multiplet calculation of Fe 2*p* XAS reveals that doped Fe-ion replaces the tetrahedral Zn-sites in ZnO. O 1*s* XAS spectra are measured to probe the hybridized O 2*p* and Zn 3*d*4*s*/Fe 3*d* orbitals. Fe L_2-RIXS measurements indicate that higher number of charge carriers are probable for the sample made of polycrystalline ZnO compared to one made of an epitaxial ZnO. Also, a high Fe-ion dose is likely to form FeO clusters in the sample.

REFERENCES

1. S. Jin, T. H. Tiefel, M. McCormack, R. A. Fastnacht, R. Ramesh, and L. H. Chen, *Science* **264**, 413 (1994).

2. C. Zener, *Phys. Rev.* **82**, 403 (1951).

3. H. Dulli, P. A. Dowben, S.-H. Liou, and E. W. Plummer, *Phys. Rev. B* **62**, R14 629 (2000).

4. J.-H. Park, E. Vescovo, H.-J. Kim, C. Kwon, R. Ramesh, and T. Venkatesan, *Phys. Rev. Lett*. **81**, 1953 (1998).

5. Ll. Abad, B. Martínez, and Ll. Balcells, *Appl. Phys. Lett*. **87**, 212502 (2005).

6. L. Abad, B. Martínez, S. Valencia, A. Gaupp, W. Gudat, and L. Balcells, *Adv. Sci. Technol*. **52**, 87 (2006).

7. S. Valencia, A. Gaupp, W. Gudat, Ll. Abad, Ll. Balcells, and B. Martínez, *Appl. Phys. Lett*. **90**, 252509 (2007).

8. M. J. Calderón, L. Brey, and F. Guinea, *Phys. Rev. B* **60**, 6698 (1999).

9. C. N. Borca, B. Xu, T. Komesu, H. K. Jeong, M. T. Liu, S.-H. Liou, S. Stadler, Y. Idzerda, and P. A. Dowben, *Europhys. Lett.* **56**, 722 (2001).

10. S. Maekawa and U. Gäfvert, *IEEE Trans. Magn.* **MAG-18**, 707 (1982).

11. M. P. de Jong, I. Bergenti, V. A. Dediu, M. Fahlman, M. Marsi, and C. Taliani, *Phys. Rev. B* **71**, 014434 (2005).

12. M. P. de Jong, I. Bergenti, W. Osikowicz, R. Friedlein, V. A. Dediu, C. Taliani, and W. R. Salaneck, *Phys. Rev. B* **73**, 052403 (2006).

13. S. Valencia, A. Gaupp, W. Gudat, Ll. Abad, Ll. Balcells, A. Cavallaro, B. Martínez, and F. J. Palomares, *Phys. Rev. B* **73**, 104402 (2006).

14. M. F. Hundley and J. J. Neumeier, *Phys. Rev. B* **55**, 11511 (1997).

15. S. M. Butorin, J.-H. Guo, M. Magnuson, P. Kuiper, and J. Nordgren, *Phys. Rev. B* **54**, 4405 (1996).

16. B. Gilbert, B. H. Frazer, A. Belz, P. G. Conrad, K. H. Nealson, D. Haskel, J. C. Lang, G. Srajer, and G. D. Stasio, *J. Phys. Chem. A* **107**, 2839 (2003).

17. G. Ghiringhelli, A. Piazzalunga, X. Wang, A. Bendounan, H. Berger, F. Bottegoni, N. Christensen, C. Dallera, M. Grioni, J.-C. Grivel, M. M. Sala, L. Patthey, J. Schlappa, T. Schmitt, V. Strocov, and L. Braicovich, *Eur. Phys. J. Special Topics* **169**, 199 (2009).

18. L. A. J. Garvie and A. J. Craven, *Phys. Chem. Minerals* **21**, 191 (1994).

19. J. Kawai, Y. Mizutani, T. Sugimura, M. Sai, T. Higuchi, Y. Harada, Y. Ishiwata, A. Fukushima, M. Fujisawa, M. Watanabec, K. Maeda, S. Shin, and Y. Gohshi, *Spectr. Acta B* **55**, 1385 (2000).

20. S. P. Cramer, F. M. F. de Groot, Y. Ma, C. T. Chen, F. Sette, C. A. Kipke, D. M. Eichhorn, M. K. Chan, W. H. Armstrong, E. Libby, G. Christou, S. Brooker, V. McKee, O. C. Mullins, and J. C. Fuggle, *J. Am. Chem. Soc.* **113**, 7937 (1991).

21. H. K. Schmid and W. Mader, *Micron* **37**, 426 (2006).

22. R. Janisch, P. Gopal, and N. A. Spaldin, *J. Phys.:Condens. Matter* **17**, R657 (2005).

23. P. Sharma, A. Gupta, K. V. Rao, F. J. Owens, R. Sharma, R. Ahuja, J. M. O. Guillen, B. Johansson, and G. A. Gehring, *Nat. Mater.* **2**, 673 (2003).

24. A. Y. Polyakov, A. V. Govorkov, N. B. Smirnov, N. V. Pashkova, S. J. Pearton, K. Ip, R. M. Frazier, C. R. Abernathy, D. P. Norton, J. M. Zavada, and R. G. Wilson, *Mater. Sci. Semicond. Process.* **7**, 77 (2004).

25. K. Ueda, H. Tabata, and T. Kawai, *Appl. Phys. Lett.* **79**, 988 (2001).

26. Y. M. Cho, W. K. Choo, H. Kim, D. Kim, and Y. Ihm, *Appl. Phys. Lett.* **80**, 3358 (2002).

27. A. A. Abrikosov and L. P. Gorkov, *Sov. Phys. JETP* **16**, 1575 (1963).

28. T. Ditel, H. Ohno, and F. Matsukura, *Phys. Rev. B* **63**, 195205 (2001).

29. A. Chattopadhyay, S. D. Sarma, and A. J. Millis, *Phys. Rev. Lett.* **87**, 227202 (2001).

30. P. A. Wolff, R. N. Bhatt, and A. C. Durst, *J. Appl. Phys.* **79**, 5196 (1996).

31. A. Kaminski and S. D. Sarma, *Phys. Rev. Lett.* **88**, 247202 (2002).

32. M. Berciu and R. N. Bhatt, *Phys. Rev. Lett.* **87**, 107203 (2001).

33. A. L. Chudnovskiy and D. Pfannkuche, *Phys. Rev. B* **65**, 165216 (2002).

34. H. C. Pollock, *Am. J. Phys.* **51 (3)**, 278 (1983).

35. D. Attwood, *Soft X-rays and Extreme Ultraviolet Radiation* (Cambridge University Press, U.S.A., 1999).

36. Canadian Light Source, *How does the CLS synchrotron work*, http://www.lightsource.ca/education/pdf/materials/1.2_How_does_the_CLS_Synchrotron_work.pdf.

37. J. Cutler, E. Hallin, M. de Jong, W. Thomlinson, and T. Ellis, *Nucl. Instrum. Methods A* **582**, 11 (2007).

38. Canadian Light Source, http://www.lightsource.ca/.

39. T. Regier, J. Krochak, T. K. Sham, Y. F. Hu, J. Thompson, and R. I. R. Blyth, *Nucl. Instrum. Methods A* **582**, 93 (2007).

40. Canadian Light Source, *Layout of the SGM beamline*, www.lightsource.ca/brochures/pdf/activity_report_2007/65_Sham.

41. J. J. Jia, T. A. Callcott, J. Yurkas, A. W. Ellis, F. J. Himpsel, M. G. Samant, J. Stöhr, D. L. Ederer, J. A. Carlisle, E. A. Hudson, L. J. Terminello, D. K. Shuh, and R. C. C. Perera, *Rev. Sci. Instrum.* **66**, 1394 (1995).

42. Advanced Light Source, *High Resolution and Flux for Materials and Surface Science, Beamline 8.0.1*, 2009, http://www-als.lbl.gov/als/als_users_bl/8.0.1-Overview.pdf.

43. Advanced Light Source, *Soft X-ray Fluorescence (SXF) Spectrometer, Beamline 8.0.1*, 2003, http://www-als.lbl.gov/als/als_users_bl/8.0.1-SXF.pdf.

44. *X-ray absorption spectroscopy*, http://www.chem.ucalgary.ca/research/groups/faridehj/xas.pdf.

45. A. Kotani and S. Shin, *Rev. Mod. Phys.* **73**, 203 (2001).

46. P. Glatzel, U. Bergmann, J. Yano, H. Visser, J. H. Robblee, W. Gu, F. M. F. de Groot, G. Christou, V. L. Pecoraro, S. P. Cramer, and V. K. Yachandra, *J. Am. Chem. Soc.* **126**, 9946 (2004).

47. C. David Sherrill, *An Introduction to Hartree-Fock Molecular Orbital Theory* (2000), http://vergil.chemistry.gatech.edu/notes/hf-intro/hf-intro.pdf.

48. S. Asada, C. Satako, and S. Sugano, *J. Phys. Soc. Jap.* **37**, 855 (1975).

49. T. Yamaguchi and S. Sugano, *J. Phys. Soc. Jap.* **42**, 1949 (1977).

50. R. P. Gupta and S. K. Sen, *Phys. Rev. B.* **10**, 71 (1974).

51. R. P. Gupta and S. K. Sen, *Phys. Rev. B.* **12**, 15 (1975).

52. S. Asada and S. Sugano, *J. Phys. Soc. Jap.* **41**, 1291 (1976).

53. B. T. Thole, G. van der Laan, J. C. Fuggle, G. A. Sawatzky, R. C. Karnatak, and J.-M. Esteva, *Phys. Rev. B.* **32**, 5107 (1985).

54. R. D. Cowan, *The Theory of Atomic Structure and Spectra* (Univ. of California Press, Berkeley, 1981).

55. R. D. Cowan, *J. Opt. Soc. Am.* **58**, 808 (1968).

56. B. T. Thole, R. D. Cowan, G. A. Sawatzky, J. Fink, and J. C. Fuggle, *Phys. Rev. B.* **31**, 6856 (1985).

57. F. de Groot, *Coordination Chemistry Reviews* **249**, 31 (2005).

58. F. M. F. de Groot and J. C. Fuggle, *Phys. Rev. B.* **42**, 5459 (1990).

59. F. de Groot, *Chem. Rev.* **101**, 1779 (2001).

60. M. Weissbluth, *Atoms and Molecules* (Plenum Press, New York, 1978).

61. P. H. Butler, *Point Group Symmetry, Applications, Methods, and Tables* (Plenum Press, New York, 1981).

62. J. R. Derome and W. T. Sharp, *J. Math. Phys.* **6**, 1584 (1965).

63. P. H. Butler and B. G. Wybourne, *Int. J. Quantum Chem.* **10**, 581 (1976).

64. S. Sugano, Y. Tanabe, and H. Kamimura, *Multiplets of Transition Metal Ions in Crystals* (Academic Press, New York, 1970).

65. G. W. Coulston, S. R. Bare, H. Kung, K. Birkeland, G. K. Bethke, R. Harlow, N. Herron, and P. L. Lee, *Science* **275**, 191 (1997).

66. M. Fernandez-Garcia, C. M. Alvarez, and G. L. Haller, *J. Phys.Chem.* **99**, 12565 (1995).

67. S. R. Wasserman, R. E. Winans, and R. McBeth, *Energy & Fuels* **10**, 392 (1996).

68. S. R. Wasserman, J. *Phys. IV France* **7**, C2-203 (1997).

69. S. R. Wasserman, L. Soderholm, and U. Staub, *Chem. Mater.* **10**, 559 (1998).

70. E. R. Malinowski and D. G. Howery, *Factor Analysis in Chemistry* (John Wiley and Sons, New York, 1980).

71. G. N. George, *EXAFSPAK*, http://ssrl.slac.stanford.edu/exafspak.html.

72. A. M. Balbashov and S. K. Egorov, *J. Crystal Growth* **52**, 498 (1981).

73. D. Shulyateva, S. Karabasheva, A. Arsenova, Y. Mukovskii, and S. Zverkov, *J. Crystal Growth* **237-239**, 810 (2002).

74. W. Jiang, X. Zhou, and G. Williams, *Phys. Rev. Lett.* **99**, 177203 (2007).

75. R. Niewa, Z. Hu, C. Grazioli, U. Röβler, M. S. Golden, M. Knupfer, J. Fink, H. Giefers, G. Wortmann, F. M. F. de Froot, and F. J. DiSalvo, *J. Alloys Compd.* **346**, 129 (2002).

76. G. van der Laan and I. W. Kirkman, *J. Phys.:Condens. Matter* **4**, 4189 (1992).

77. M. Abbate, F. M. F. de Groot, J. C. Fuggle, A. Fujimori, O. Strebel, F. Lopez, M. Domke, G. Kaindl, G. A. Sawatzky, M. Takano, Y. Takeda, H. Eisaki, and S. Uchida, *Phys. Rev. B* **46**, 4511 (1992).

78. W. Gudat and C. Kunz, *Phys. Rev. Lett.* **29**, 169 (1972).

79. C. Mitra, Z. Hu, P. Raychaudhuri, S. Wirth, S. I. Csiszar, H. H. Hsieh, H. J. Lin, C. T. Chen, and L. H. Tjeng, *Phys. Rev. Lett.* **67**, 092404 (2003).

80. *X-ray attenuation length of a solid*, http://henke.lbl.gov/optical constants/.

81. F. M. F. de Groot, M. Grioni, J. C. Fuggle, J. Ghijsen, G. A. Sawatzky, and H. Petersen, *Phys. Rev. B* **40**, 5715 (1989).

82. M. M. Grush, J. Chen, T. L. Stemmler, S. J. George, C. Y. Ralston, R. T. Stibrany, A. Gelasco, G. Christou, S. M. Gorun, J. E. Penner-Hahn, and S. P. Cramer, *J. Am. Chem. Soc.* **118**, 65 (1996).

83. S. J. George, J. van Elp, J. Chen, Y. Ma, C. T. Chen, J.-B. Park, M. W. W. Adams, B. G. Searle, F. M. F. de Groot, J. C. Fuggle, and S. P. Cramer, *J. Am. Chem. Soc*. **114**, 4426 (1992).

84. J. van Elp, G. Peng, Z. H. Zhou, S. Mukund, and M. W. W. Adams, *Phys. Rev. B* **53**, 2523 (1996).

85. C. Theil, J. van Elp, and F. Folkmann, *Phys. Rev. B* **59**, 7931 (1999).

86. J. van Elp, G. Peng, B. G. Searle, S. Mitra-Kirtley, Y.-H. Huang, M. K. Johnson, Z. H. Zhou, M. W. W. Adams, M. J. Maroney, and S. P. Cramer, *J. Am. Chem. Soc.* **116**, 1918 (1994).

87. G. Ghiringhelli, M. Matsubara, C. Dallera, F. Fracassi, A. Tagliaferri, N. B. Brookes, A. Kotani, and L. Braicovich, *Phys. Rev. B* **73**, 035111 (2006).

88. P. Glatzel, J. Yano, U. Bergmann, H. Visser, J. H. Robblee, W. Gu, F. M. F. de Groot, S. P. Cramer, and V. K. Yachandra, *J. Phys. Chem. Solids* **66**, 2163 (2005).

89. S. M. Butorin, *J. Electron Spectrosc. Relat. Phenom.* **110-111**, 213 (2000).

90. P. Kuiper, J.-H. Guo, C. Såthe, L.-C. Duda, J. Nodgren, J. J. M. Pothuizen, F. M. F. de Groot, and G. A. Sawatzky, *Phys. Rev. Lett.* **80**, 5204 (1998).

91. S. Gautam, S. Kumar, P. Thakur, K. H. Chae, R. Kumar, B. H. Koo, and C. G. Lee, *J. Phys. D:Appl. Phys.* **42**, 175406 (2009).

92. Y. Lin, D. Jiang, F. Lin, W. Shi, and X. Ma, *Journal of Alloys and Compounds* **436**, 30 (2007).

93. D. Karmakar, S. K. Mandal, R. M. Kadam, P. L. Paulose, A. K. Rajarajan, T. K. Nath, A. K. Das, I. Dasgupta, and G. P. Das, *Phys Rev B* **75**, 144404 (2007).

94. J. W. Chiou, K. P. K. Kumar, J. C. Jan, H. M. Tsai, C. W. Bao, W. F. Pong, F. Z. Chien, M.-H. Tsai, I.-H. Hong, R. Klauser, J. F. Lee, J. J. Wu, and S. C. Liu, *Appl. Phys. Lett.* **85**, 3220 (2004).

95. G. S. Chang, E. Z. Kurmaev, D. W. Boukhvalov, L. D. Finkelstein, S. Colis, T. M. Pedersen, A. Moewes, and A. Dinia, *Phys. Rev. B* **75**, 195215 (2007).

96. S. Krishnamurthy, C. McGuinness, L. S. Dorneles, M. Venkatesan, J. M. D. Coey, J. G. Lunney, C. H. Patterson, K. E. Smith, T. Learmonth, P.-A. Glans, T. Schmitt, and J.-H. Guo, *J. Applied Phys.* **99**, 08M111 (2006).

97. E. Z. Kurmaev, A. L. Ankudinov, J. J. Rehr, L. D. Finkelstein, P. F. Karimov, and A. Moewes, *J. Electron Spectrosc. Relat. Phenom.* **148**, 1 (2005).

98. V. I. Grebennikov, *Surface Investigations: X-ray, Synchrotron and Neutron Techniques* **11**, 41 (2002).

99. J. L. Zhao, W. Zhang, X. M. Li, J. W. Feng, and X. Shi, *J. Phys.:Condens. Matter* **18**, 1495 (2006).

100. K. Potzger, S. Zhou, H. Reuther, K. Kuepper, G. Talut, M. Helm, and J. Fassbender, *Appl. Phys. Lett.* **91**, 062107 (2007).

APPENDIX A

XAS input files

A group of programs written by B. T. Thole and later modified by Jason Sadowski, Mark Hlady, and Adrian Hunt at the University of Saskatchewan are used to calculate atomic XAS. Three programs (RCN2, RCG2, and RAC2) and input files are used to create an ".ora" file which is then used as input for the final program called "Crystal field atomic multiplet calculation.exe". The programs RCN2, RCG2, and RAC2 run with command prompt so that one can specify the input file to be used.

The first program is **RCN2**
Input file: *.rcn
Output file: *.rcf

*.rcn has the following format and can be edited with notepad. Following is an example of this input file for Mn^{2+}. The colored entries are edited according to the element to be calculated.

```
22 -9    2   10  1.0    5.E-06    1.E-09-2   130    1.0  0.65  0.0 0.50 0.0  0.70
  25     Mn2+ 2p06 3d05        2P06 3D05
  25     Mn2+ 2p05 3d06        2P05 3D06   -1
```

Cyan Section: The atomic number of the element.
Yellow Section: Simply a label for the species.
Green Section: The specific electronic configuration of the element.

The output of the above input file (*.rcn) is a "*.rcf" file, which has the following format. It has to be edited with notepad to use it as an input for the second program called RCG2. We change 00 to 14, 4 to 2, highlighted zeros to 3, and scaling factors. Once it is edited the "*.rcf" must be renamed to "*.rcg".

```
  10    1    0   00    4    4    1    1 SHELL00000000 SPIN00000000 INTER8
   0                   80998080          8065.47800     0000000
   1     2 1 12 1 10         00      9 00000000 0 8065.4790 .00       1
P 6  D 5
P 5  D 6
Mn2+ 2p06 3d05     4    0.0000   10.3161    6.4141    0.0402    0.0000HR99999999
Mn2+ 2p05 3d06     8  644.6170   11.1551    6.9431    6.8462    0.0532HR99999999
   6.3213    4.6064    2.6184
Mn2+ 2p06 3d05      Mn2+ 2p05 3d06        -0.20620( 2P//R1// 3D) 1.000HR  35-100
                -99999999.
  -1
```

The second program is **RCG2**

Input file: *.rcg

Output file: *.m14

This output file (*.m14) is directly used as one of the input for the third program RAC2. RAC2 requires another input file called '*.rac' with the format specified below. This *.rac file defines the crystal field and the format varies depending on the symmetry. The strength parameter of the crystal field is highlighted. It is in units of 0.304 eV. If the crystal field value is positive then it is considered of octahedral symmetry and on the other hand if the value is negative then the crystal is considered of tetrahedral symmetry. Following format of the *.rac file stands for an octahedral symmetry.

```
Y
   % vertical 1 1
 butler O3
 to    Oh
 endchain
 actor   0+ HAMILTONIAN ground  PRINTEIG
  OPER HAMILTONIAN
    BRANCH 0+ > 0 0+ 1.0
  OPER SHELL2
    BRANCH 4+ > 0 0+ +0.9
 actor   0+ HAMILTONIAN excite  PRINTEIG
  OPER HAMILTONIAN
    BRANCH 0+ > 0 0+ 1.0
  OPER SHELL2
    BRANCH 4+ > 0 0+ +0.9
 actor   1- left        transi PRINTTRANS
   oper MULTIPOLE
     branch  1- > 0 1- 1.000
RUN
```

The third program is **RAC2**

Input files: *.rac and *.m14

Output file: *.ora

Now, the output file of the RAC2 (*.ora) is used as input for the program “Crystal field atomic multiplet calculation.exe”. The “Crystal field atomic multiplet calculation.exe” program runs and requests input as follows. It is shown below with the highlighted inputs.

```
-----------------------------------------------
    Crystal Field Atomic Multiplet Program
-----------------------------------------------
Authors: Jason Sadowski, Mark Hlady, Adrian Hunt

Would you like to use an existing filter file?
(y/n)
n

Please enter input filename : mn2plus.ora
Program Options:
1)For XAS calculatoins: Simple data formatting and broadening
2)For RIXS calculations: Data formatting with Kramers-Heisenberg formula
Enter 1 or 2
1
Is this a racah (crystal field multiplet) or
bander (charge transfer) output file?
Enter 1 for racah or 2 for bander.
1

For the file, filter2.dat,
Do you wish to select only certain states or transitions?
(y/n)
y

Please select which:
1) states
2) Transitions
Enter 1 or 2
1
```

Please indicate which group to select from:

1)initial E

2)final E

Enter 1 or 2

1

Spectra has found the following initial state states.

The energy values of those states are displayed after the colon.

^S0+: 5.6276 2.975 2.1987 0.8333 0.8081 0.4937 0.3533
0.0248 -0.0011 -0.0325 -0.0844 -0.4855 -0.8728 -0.9165 -1.0015
-1.3884 -1.4191 -1.6075 -2.1752 -2.197 -2.2865 -5.3133

S1+: 5.6396 5.6318 4.8277 2.9732 2.9596 2.9419 2.2098
2.1885 0.8332 0.7848 0.4741 0.4344 0.4222 0.338 0.2384
0.2058 0.1695 0.0127 0.0085 -0.0124 -0.0295 -0.0344 -0.0686
-0.1365 -0.3088 -0.4039 -0.8573 -0.8809 -0.9179 -0.9739 -1.3914
-1.4193 -1.4299 -1.6023 -1.6104 -2.174 -2.1755 -2.1865 -2.1924
-2.2824 -2.2853 -5.3133

S0+: 4.8314 2.9897 2.9644 1.4524 0.8316 0.4426 0.3663
0.2071 0.1519 0.0115 -0.0382 -0.144 -0.8436 -0.8987 -1.399
-1.4398 -1.5927 -2.1739 -2.1872 -2.2789

Please enter the initial state(s) you wish to consider:

Include selected energies on the same line as the symbol(separated by a space),

if any.

Entering 'xx' on a new line quits.

^S0+ -5.3133

S1+ -5.3133

xx

In which format would you like your data?

1) Energy vs. rate only

2) All transition data

Enter 1 or 2

1

Generating filter2.dat...

Please indicate broadening type:

1) Gaussian

2) Lorentzian

Enter 1 or 2

1

Name of broadened file to write: Mn2

Broadening full width at half maximum: 0.5

There are 943 lines

in the energy range

621.805 eV -->685.569 eV.

How many points to plot in this range (3999 max)?3999

The name of the output file is defined in the prompt, “Name of broadened file to write: Mn2” and it appears in the same folder when the calculation is done. The program thus gives an output file with the chosen name, which can be plotted using “Origin”. For the best result, we adjust different parameters e.g. scaling factors in the *.rcg file, crystal field value in the *rac file, and broadening factor in the “Crystal field atomic multiplet calculation.exe”. The obtained spectra are shifted along the energy axis to match with the experiment.

Appendix B

RIXS input files

To calculate RIXS, an XAS spectrum for that element is calculated first so that the excitation energies for RIXS calculations can be chosen from it. In this thesis RIXS are calculated without considering the crystal field, and are calculated using the program called Basis state edition (BSE) which is a little different from the above mentioned crystal field multiplet calculation program described in appendix A. Here BSE is used to first calculate the XAS and then to calculate the RIXS. Three programs (rcn.exe, rcn2.exe, and rcglusask.exe) are called in a sequence using the batch file called "run with cfp.bat." The codes in this section are originally written by Robert Cowan. Two input files are used in this case namely, "in36" and "IN2". Sample input files for Mn^{2+} is given below.

The input file "in 36" has following format and is edited (highlighted sections) with notepad as required by the element to be calculated. The top line describes the initial state of the atom and the lower line describes the excited state of the atom. Taken together these two lines tell the program what transitions to calculate.

```
2  -9    2   10  0.2    5.e-08    1.e-11-2   190    1.0 0.65  0.0 0.00
  25    3Mn II  2p63d5     2p06 3d05
  25    3Mn II  2p53d6     2p05 3d06
  -1
```

Cyan Section: The atomic number of the element.
Magenta Section: The number one greater than the oxidation state of the element.
Yellow Section: Simply a label for the species.
Green Section: The specific electronic configuration of the element.

The other input file “IN2” has the following format. The scaling factors (highlighted green section) are modified to obtain the best fit to the experiment.

g5inp1 0 0000 0.000 000 0000000 00000000 8099808080.0000 08229
-1

The program “run with cfp.bat” uses ‘in36’ and ‘in2’ as input files and yield ‘outg11’ as the primary output file, which is finally used by the program BSE to calculate XAS and RIXS. A sample XAS calculation for Mn^{2+} using BSE is given below with the highlighted input entries.

#
Spectra Calculator v2.0
#

Would you like to use an existing filter file?
(y/n)
n

Please enter input filename : outg11

Program Options:
1) Version A -- Simple data formatting and broadening
2) Version B -- Data formatting with Kramers-Heisenberg formula calculation
Enter 1 or 2
1

Scanning file...
Generating filter.dat...

For the file, filter2.dat,

Do you wish to select only certain terms or transitions?

(y/n)

y

Please select which:

1) Terms

2) Transitions

Enter 1 or 2

1

Please indicate which group to select from:

1)initial E

2)final E

Enter 1 or 2

1

Spectra has found the following initial state terms:

6S 4P 4G 4D 2I 4F 2H 2S 2F 2G

2P 2D

Please enter the term(s) to use as a mask:

Include selected j-values on the same line (separated by a space), if any.

Entering 'xx' on a new line quits.

6S

xx

In which format would you like your data?

1) Energy vs. rate only

2) All transition data

Enter 1 or 2

1

Generating filter2.dat...

Please indicate broadening type:

1) Gaussian

2) Lorentzian

Enter 1 or 2

1

Name of broadened file to write: Mn2

Broadening full width at half maximum: 0.5

There are 110 lines

in the energy range

622.606 eV -->683.204 eV.

How many points to plot in this range (3999 max)? 3999

The output file appears in the same folder with the specified name (in this case, Mn2). This output file is plotted in Origin to obtain the XAS spectrum. Now, to calculate the RIXS one can choose excitation energies from the obtained XAS data, and run the program BSE again using the version B (Data formatting with Kramers-Heisenberg formula) in the program option. A sample calculation for Mn^{2+} RIXS at 642.7 eV (feature corresponding to the 640.8 eV in the experiment) is shown below.

#

Spectra Calculator v2.0

#

Would you like to use an existing filter file?

(y/n)

n

Please enter input filename : outg11

Program Options:

1) Version A -- Simple data formatting and broadening

2) Version B -- Data formatting with Kramers-Heisenberg formula calculation

Enter 1 or 2

2

Scanning file...

Generating filter.dat...

Spectra has found the following initial state terms:

6S 4P 4G 4D 2I 4F 2H 2S 2F 2G

2P 2D

Please enter your selected terms.

Include selected j-values on the same line (separated by a space), if any.

Entering 'xx' on a new line quits.

6S

xx

Spectra has found the following intermediate terms with j-values.
Each intermediate state is seperated by a vertical line.

4P 2.5 | 2D 2.5 | 2G 3.5 | 4P 1.5 | 4S 1.5 | 4G 3.5 | 2F 2.5 | 2F 3.5 |
4G 2.5 | 2P 1.5 |
2D 1.5 | 4H 3.5 | 4D 1.5 | 4D 2.5 | 4D 3.5 | 4F 1.5 | 4F 2.5 | 4F 3.5 |
6P 1.5 | 6P 2.5 |
6D 1.5 | 6D 2.5 | 6F 3.5 |

Please enter your selected terms or basis state labels.
Include selected j-values on the same line (separated by a space), if any.
Entering 'xx' on a new line quits, entering 'all' selects all.
all

Spectra has found the following basis-state labels:

For the 6S 2.5 to 4P 2.5 transition, the basis-state labels are:

(3P)

For the 6S 2.5 to 2D 2.5 transition, the basis-state labels are:
(1F) (3P) (3F) (3D) (1D)

For the 6S 2.5 to 2G 3.5 transition, the basis-state labels are:
(1F) (3H) (1G) (3F)
(3G)

For the 6S 2.5 to 4P 1.5 transition, the basis-state labels are:
(3P) (3D)

For the 6S 2.5 to 4S 1.5 transition, the basis-state labels are:
(3P)

For the 6S 2.5 to 4G 3.5 transition, the basis-state labels are:
(3F) (3H) (3G)

For the 6S 2.5 to 2F 2.5 transition, the basis-state labels are:
(1D) (3G) (1F)
(1G) (3F) (3D)

For the 6S 2.5 to 2F 3.5 transition, the basis-state labels are:
(1G) (3F) (1D) (1F) (3D) (3G)

For the 6S 2.5 to 4G 2.5 transition, the basis-state labels are:
(3F)
(3H) (3G)

For the 6S 2.5 to 2P 1.5 transition, the basis-state labels are:
(1S) (1D) (3D) (3P)

For the 6S 2.5 to 2D 1.5 transition, the basis-state labels are:
(1D) (3D) (1F) (3P)
(3F)

For the 6S 2.5 to 4H 3.5 transition, the basis-state labels are:
(3G) (3H)

For the 6S 2.5 to 4D 1.5 transition, the basis-state labels are:
(3P) (3D) (3F) (5D)
For the 6S 2.5 to 4D 2.5 transition, the basis-state labels are:
(3D) (3F) (3P)

(5D)

For the 6S 2.5 to 4D 3.5 transition, the basis-state labels are:
(3F) (3P) (5D)

For the 6S 2.5 to 4F 1.5 transition, the basis-state labels are:
(3D) (3F) (3G) (5D)

For the 6S 2.5 to 4F 2.5 transition, the basis-state labels are:
(3D) (3F)
(3G) (5D)

For the 6S 2.5 to 4F 3.5 transition, the basis-state labels are:
(3D) (3F) (5D)

For the 6S 2.5 to 6P 1.5 transition, the basis-state labels are:
(5D)

For the 6S 2.5 to 6P 2.5 transition, the basis-state labels are:
(5D)

For the 6S 2.5 to 6D 1.5 transition, the basis-state labels are:
(5D)

For the 6S 2.5 to 6D 2.5 transition, the basis-state labels are:
(5D)

For the 6S 2.5 to 6F 3.5 transition, the basis-state labels are:
(5D)
This part of the program allows you to choose the basis state labels.
If you want to use all labels, type 'all'.

If you wish to choose basis state labels, then enter the initial state,
followed by the j-value, then the intermediate state and its j value,
finally all desired basis state labels for that transition. Repeat for all
desired transitions. Remember to put spaces between everything. The order
of the basis state labels is irrelevant.

An 'xx' on a line finishes your list.
all

Are you using a separate file for final transitions?
(y/n)
n

Spectra has found the following final terms with j-values.
Each final state is seperated by a vertical line.

6S 2.5 | 4G 2.5 | 4G 3.5 | 4P 2.5 | 4P 1.5 | 4D 3.5 | 4D 1.5 | 4D 2.5 | 4G 4.5 |
4P 0.5 |
4F 3.5 | 4F 2.5 | 4F 1.5 | 4D 0.5 | 2F 2.5 | 2F 3.5 | 4F 4.5 | 2H 4.5 | 2G 3.5 |
2S 0.5 |
2G 4.5 | 2P 1.5 | 2D 2.5 | 2D 1.5 | 2P 0.5 |

Please enter your selected terms or basis state labels.
Include selected j-values on the same line(separated by a space), if any.
Entering 'xx' on a new line quits, entering 'all' selects all.
all

Please select the energy of the incoming photons:
642.7

Please select the broadening factor gamma:

0.5

Performing calculation and sort...

Writing to file kh.dat...

Please indicate broadening type:

1) Gaussian

2) Lorentzian

Enter 1 or 2

1

Name of broadened file to write: Mn642.7

Broadening full width at half maximum: 0.5

There are 37865 lines

in the energy range

612.814 eV -->667.453 eV.

How many points to plot in this range (3999 max)?3999

Program usually takes a few minutes to calculate the output file. The output file with the specified name “Mn642.7” appears in the same folder where the programs and input files exist. To obtain a best fit to the experiment, scaling factors and broadening factors are varied.